

Research paper

From mechanical modeling to seismic imaging of faults: A synthetic workflow to study the impact of faults on seismic

Charlotte Botter^{a,*}, Nestor Cardozo^a, Stuart Hardy^b, Isabelle Lecomte^c, Alejandro Escalona^a^a Department of Petroleum Engineering, University of Stavanger, 4036 Stavanger, Norway^b Institució Catalana de Recerca i Estudis Avançats (ICREA), Catalonia, Spain^c NORSAR, Gunnar Randers vei 15, 2007 Kjeller, Norway

ARTICLE INFO

Article history:

Received 16 December 2013

Received in revised form

19 May 2014

Accepted 25 May 2014

Available online 5 June 2014

Keywords:

Faults

Geomechanical modeling

Finite strain

Seismic properties

Seismic modeling

Seismic interpretation

ABSTRACT

Although typically interpreted as 2D surfaces, faults are 3D narrow zones of highly and heterogeneously strained rocks, with petrophysical properties differing from the host rock. Here we present a synthetic workflow to evaluate the potential of seismic data for imaging fault structure and properties. The workflow consists of discrete element modeling (DEM) of faulting, empirical relations to modify initial acoustic properties based on volumetric strain, and a ray-based algorithm simulating prestack depth migration (PSDM). We illustrate the application of the workflow in 2D to a 100 m displacement normal fault in a kilometer size sandstone-shale sequence at 1.5 km depth. To explore the effect of particle size on fault evolution, we ran two DEM simulations with particle assemblages of similar bulk mechanical behavior but different particle size, one with coarse (1–3 m particle radii) and the other with fine (0.5–1.5 m particle radii) particles. Both simulations produce realistic but different fault geometries and strain fields, with the finer particle size model displaying narrower fault zones and fault linkage at later stages. Seismic images of these models are highly influenced by illumination direction and wave frequency. Specular illumination highlights flat reflectors outside the fault zone, but fault related diffractions are still observable. Footwall directed illumination produces low amplitude images. Hanging wall directed illumination images the shale layers within the main fault segment and the lateral extent of fault related deformation. Resolution and the accuracy of the reflectors are proportional to wave frequency. Wave frequencies of 20 Hz or more are necessary to image the different fault structure of the coarse and fine models. At 30–40 Hz, there is a direct correlation between seismic amplitude variations and the input acoustic properties after faulting. At these high frequencies, seismic amplitude variations predict both the extent of faulting and the changes in rock properties in the fault zone.

© 2014 Elsevier Ltd. All rights reserved.

1. Introduction

Faults play a key role in restricting or enhancing fluid flow in reservoirs. Although commonly represented as 2D surfaces in reservoir models, faults are actually narrow zones or volumes of highly and heterogeneously strained rocks, with petrophysical properties differing from those of the host rock (Faulkner et al., 2010 and references therein). Faults are complex and their 3D structure and rock properties distribution depend on factors such as host lithology and stratigraphy (Davatzes et al., 2005; Eichhubl

et al., 2005; Bastesen and Braathen, 2010), depth of burial at time of faulting (Fisher and Knipe, 1998), initial fault array geometry and structural evolution (Childs et al., 2009), and diagenesis (Solum et al., 2010). Figure 1a illustrates the differences between an actual fault (Fig. 1a, left), and its standard 2D reservoir model representation (Fig. 1a, right). The structures and rocks inside the fault volume affect reservoir connectivity, and can either stop or allow fluid flow depending on their 3D geometry, distribution, and petrophysical properties. 3D fault structure and internal petrophysical properties are therefore primary controls on fluid flow in faulted reservoirs, determining fault-sealing capacity over geologic and production time scales (Faulkner et al., 2010 and references therein). This has major implications in hydrocarbon exploration and production, CO₂ storage, hydrogeological and geothermal systems (e.g., Wibberley et al., 2008).

* Corresponding author.

E-mail addresses: charlotte.botter@gmail.com, charlotte.botter@uis.no (C. Botter).

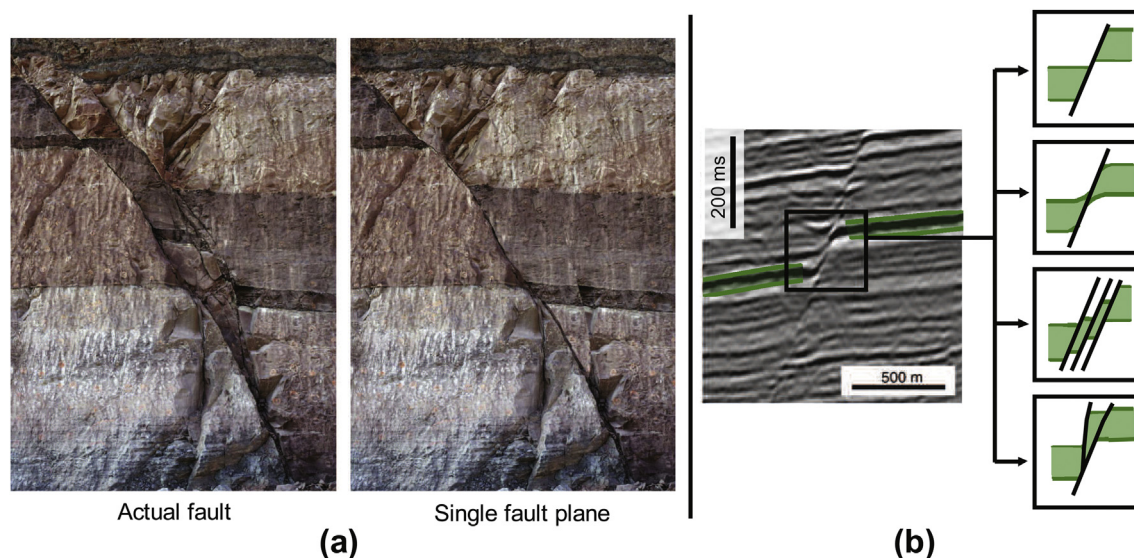


Figure 1. Examples of faults in outcrop (a) and seismic (b). (a) Actual fault (left) and modified picture with a single fault plane (right). This situation can be representative of scales going from m to km (actual and modified pictures from Haakon Fossen, <http://folk.uib.no/nglhe>). (b) Seismic profile of a fault with four possible interpretations resulting in different assessments of reservoir connectivity (modified from Wibberley et al., 2008).

Despite the impact of faults on reservoir connectivity, we still lack the understanding to fully represent them in reservoir models (Manzocchi et al., 2010). Much of what we know about the structure and internal properties of faults comes from outcrop studies. Field studies of exceptional fault outcrops have given unprecedented detail of the structure and properties of faults in 2D (e.g., Eichhubl et al., 2005) and 3D (e.g., Foxford et al., 1998), as well as an understanding of the physical and chemical processes operating in faults. These studies have also highlighted the complexity of faults in 3D (e.g., Childs et al., 1996, their Fig. 3). Outcrop data, however, mostly consist of small-scale cm to tens of m displacement faults (e.g., Childs et al., 2009, their Fig. 4). For specific combinations of lithology and fault displacement there are a limited number of outcrops and sometimes only incomplete 2D sections. Relationships derived from this small-scale outcrop dataset are often extrapolated to larger scales, although there are some concerns about the validity of this extrapolation (Færseth, 2006). Faults exhibit high variability in 3D, but we still lack quantitative, statistical tools to predict this variability (Manzocchi et al., 2010).

Large-scale faults with hundreds of m to km displacement can be mapped with seismic data. In few exceptional cases there are even well core data across these faults (Aarland and Skjerven, 1998). Fault internal structure and properties, however, are at the limit of seismic resolution. Strictly speaking, fault sealing as a property over the fault volume cannot be mapped directly with seismic. One rather looks at the impact of the fault on the surrounding rock (e.g., across fault pressure differences) to infer something about the fault properties and its sealing capacity (Yielding et al., 2010). A single fault surface with fault sealing properties determined in this manner is a reasonable estimate of the flow properties across and along the fault. However, within the limits of resolution of seismic data, there is room for alternative interpretations, which are equally valid and result in different assessments of reservoir connectivity (Fig. 1b).

Most of the seismic interpretation studies target the recognition of fault networks and their organization, whilst there are not many examples in the literature examining the potential of seismic data to elucidate the complexity of fault structure and its properties in

space and time (i.e., fault evolution). A few studies focus on existing 3D seismic data using a range of seismic attributes to resolve the fault seismic response. Townsend et al. (1998) use seismic amplitude anomalies to detect small-scale faulting. Koledoye et al. (2003) decompose a large, seismically resolvable fault into segments to determine shale smearing. Dutzer et al. (2010) estimate fault architecture and fault sealing using seismic attributes in fault volumes. Long and Imber (2010, 2012) map the spatial distribution of fault related deformation using a seismic dip anomaly attribute. Iacopini and Butler (2011) and Iacopini et al. (2012) describe the geometry of complex thrust belts and associated fault damage zones by combining seismic attributes and volume based image processing and visualization techniques. Other works focus on the response of trapped waves within large fault zones in order to relate the anomalous behavior of the seismic wavefield to a possible fault zone (e.g. Ben-Zion et al., 2003; Lewis et al., 2005; Shtivelman et al., 2005). These techniques are however not applicable to standard industry seismic data and faults at large depths. Seismic characterization of fractured reservoirs is well covered in the literature, and fracture recognition (e.g., azimuthal variation in P-field, Li et al., 2003) could to some extent be extrapolated to larger fault zones. Nonetheless, despite all these studies, there is broad skepticism about the use of seismic data to characterize faults, partly because faults are at the limit of vertical and horizontal seismic resolution (Fig. 1b), and partly because standard industry seismic data are not designed to deal properly with the non-specular, back-scattered energy from faults.

The main objective of this paper is to describe a synthetic workflow to assess the potential of seismic for imaging fault structure and properties. The workflow is based on a geo-mechanical discrete element method (DEM) of faulting (Hardy et al., 2009), simple empirical relations to modify the initial acoustic properties of the model based on fault related finite strain, and a ray-based prestack depth migration (PSDM) simulator (Lecomte, 2008) to produce seismic images of the modeled fault. As a proof of concept, the workflow is investigated here in 2D, although it is possible to extend it to 3D. The DEM models the rock as an assemblage of circular rigid particles in 2D, and its main

purpose is to produce a realistic fault geometry and finite strain field. This strain field is then used to modify initial/base acoustic properties of the host rock using a simple empirical relation between acoustic properties and volumetric strain. The modified acoustic properties are used to construct a reflectivity volume, which is the input to the PSDM simulator. Parameters such as wave frequency and illumination direction and their impact on the resulting seismic image can be evaluated with the PSDM simulator. As a proof of concept, the study will focus mainly on the impact of illumination direction on the resultant seismic image, and on how the amplitude variations are related to the fault architecture and its modified acoustic properties.

Notice that the DEM is not the only way to produce a realistic picture of the fault. A digitized/parameterized schematic of a fault based on outcrop data could also suffice for this purpose. This outcrop based schematic however, will not be exempt from issues related to strain heterogeneity and most importantly upscaling of petrophysical and acoustic properties from the outcrop or laboratory to the realm of industry standard seismic acquisition at a couple of kilometers depth. We use the DEM because besides producing realistic fault architectures, it gives flexibility for imposing different displacement and stress boundary conditions, as well as allowing upscaling in terms of a continuous parameter such as strain. Practical considerations (i.e. computing limitation in the number of particles) in the DEM do not allow us to simulate faulting at the grain scale, but rather in a large fault displacement model, bulk strain at a meter size scale. Our geomechanical model does not predict the effect of fault related, grain scale processes such as disaggregation or cataclasis on rock properties. Rather we use a simple relation between bulk volumetric strain and change of acoustic properties to update the model. The ultimate proof of this approach is the production of a reflectivity volume realistic enough that contains the effects of faulting.

We illustrate the application of the workflow in 2D to a large-scale (100 m displacement) normal fault model in an interlayered sandstone-shale sequence. To evaluate the impact of particle (i.e. element) size in the DEM, we run the simulation with two assemblages of similar bulk stress–strain behavior but different particle size: one with coarser particles and another with finer particles approximately half the size of the coarser one. The finer particle size assemblage results in more strain localization and a narrower fault area. This result, which at first view seems to point up a weakness of the DEM method, actually indicates the richness and complexity of the simulated fault behavior. Just as in analogue models, for modeling materials of similar bulk behavior, fault zone thickness is controlled by particle size (Eisenstadt and Sims, 2005), so in the DEM strain localization and fault extent are controlled by particle size. We construct reflectivity grids for the two, coarse and fine particle size models, using our simple relation between change of acoustic properties and volumetric strain in the models. PSDM simulations of the two models for different wave frequencies and illumination directions, resulting in different seismic images, are presented. In an attempt to understand which combination of these parameters result in a better prediction of the structure and properties of the fault, we look in the different seismic images at the variation of seismic amplitude along interpreted reflectors, and compare it to the variation in acoustic properties along the same paths in the input reflectivity models. Overall, this exercise provides guidelines for a better characterization of faults using seismic data.

2. Methodology

Our workflow takes into consideration the complexity of fault development, the large finite strains resulting from faulting and the

impact of the overburden. The methodology is divided in three steps: 1. Geomechanical simulation using the discrete element method (DEM), 2. Empirical relations applied to the geomechanical model to modify its initial acoustic properties based on finite strain, and 3. Simulated seismic imaging (PSDM), taking into account effects in resolution and illumination. This methodology is similar to that of Couples et al. (2007), where they use a continuum finite element technique to simulate faulting, and ray-tracing (1D convolution) of the geomechanical model (with acoustic properties modified by finite strain), to produce a seismic image of the fault. Our workflow, however, has some important differences. For geomechanical modeling, we use a discontinuum, meshless technique (DEM; Hardy et al., 2009), and for seismic imaging, we use a ray-based algorithm (Lecomte, 2008) that, as opposed to 1D convolution, can handle model and survey-based effects in resolution and illumination, as well as diffracted energy (Gjøystdal et al., 2007; Lecomte, 2008; Drottning et al., 2009; Kaschwich et al., 2011).

2.1. Mechanical modeling

The DEM is a discontinuum method used to simulate the dynamic evolution of a system of discrete elements under applied forces and displacement boundary conditions. Discrete element models, in common with other numerical techniques, have both advantages and disadvantages when considering their application to geological problems (Gray et al., 2014). On one hand, modeling of high-strain deformation of brittle sedimentary cover is ideal for the discrete element technique as it is well suited to studying problems in which discontinuities (shear-zones, faults, fractures, etc.) are important. The DEM allows large deformations involving large relative displacements of individual particles and complex, abrupt boundary conditions without the need for re-meshing (Cundall and Strack, 1979; Finch et al., 2004; Egholm et al., 2007; Hardy, 2008, 2011; Thompson et al., 2010). In addition, it allows localization and the formation and linkage of faults and fractures as a natural part of the numerical scheme. However, one disadvantage of the technique lies in the necessary, but tedious and time-consuming, calibration of particle parameters to the emergent rock physical properties (Egholm et al., 2007; Holohan et al., 2011). The selection of particle parameters ultimately controls the bulk mechanical behavior of the assembly under consideration, and has to be calibrated rather than directly input as in the case of finite element or finite difference methods. The particle properties and the emergent bulk material properties are typically assessed through the use of angle of repose and biaxial tests. Such tests are performed on a subpart of the system in order to evaluate multiple sets of particle property values within acceptable runtimes (Oger et al., 1998; Finch et al., 2004; Holohan et al., 2011). Similarly, the sensitivity of models to subtle initial differences in, e.g., assembly packing is well known (Abe et al., 2011). Even with meticulous and precise work, the calibration process can lead to results slightly different from similar finite element models (Gray et al., 2014; Zhang et al., 2013). Indeed, the interaction of thousands of particles, both locally and globally, leads to situations wherein our ability to explain precisely why a particular fault or fracture grew at the expense of another is limited. Such issues also exist in analogue modeling of faulting where repeated experiments under the same boundary conditions are reasonably reproducible but not in the finer details of the fault and fracture systems (e.g. van Gent et al., 2010). The important message to be taken from any of these studies is not the precise location of an individual fault, but rather the distinctive, repeatable patterns and sequences of structural behavior emerging from multiple experiments. Bearing these factors in mind, we consider that the DEM is an appropriate method to study the process of fault formation: from initiation, through propagation and linkage,

including fault-related folding. Computational limitations on element size and/or model resolution are important, but recent, rapid advances in computational power and the parallelization of discrete element codes allow for higher resolution models.

Fault evolution has been studied by DEM modeling at large and small scales, and both at shallow and deep depths (Schöpfer et al., 2007; Egholm et al., 2008; Hardy, 2011; Terhegge et al., 2013). Here we apply the technique to large-scale faults (100 m to km fault displacement) in sedimentary-layered sequences at a few kilometers depth. The particular discrete element code employed here is a variant of the lattice solid model of Mora and Place (1993), further developed by Hardy and Finch (2005, 2006) and Hardy et al. (2009), where the rock mass is treated as an assemblage of circular particles in 2D (Fig. 2a–b). These particles are rigid, have meter-size scale (in km size simulations) and a given density. They interact with elastic, frictional, and gravitational forces (Fig. 2a–c). Imposed displacement conditions are applied to the boundary particles in order to initiate and propagate faulting in the model (Fig. 2a, bold black lines and arrows). As the assembly, these boundary particles are unbounded and frictional, and displace according to the assigned direction parallel to the fault plane. At each time step, the

total forces applied to a particle by its neighbors are used to compute its displacement. The particles are moved to their new positions by integrating their equations of motion using Newtonian physics and a velocity Verlet numerical scheme (Mora and Place, 1993). Figure 2b shows a 2D particle assemblage before (left) and after deformation (right).

To model a layered sedimentary sequence at a few kilometers depth requires some refinement of our modeling technique. Firstly, the simulation of a layered sequence comprising weak and strong materials (shale and sandstone, Fig. 2a) requires the use, and calibration, of different coefficients of interparticle friction (Fig. 2c) for each rock material. Secondly, to bring the model to reservoir depths, we must apply an overburden stress at the top of it. This is a traction component applied at the center of the particles, normal to the slope of the top surface. For each particle, the slope defined by its left and right neighbors is calculated, and the overburden traction is applied perpendicular to it (Fig. 2d). The same methodology is used in biaxial simulations for the calibration of the sandstone and shale rock materials (Section 3). In our model, there is no bonding between particles, which results in the assemblage having no tensile strength and a purely frictional behavior (Hardy, 2013).

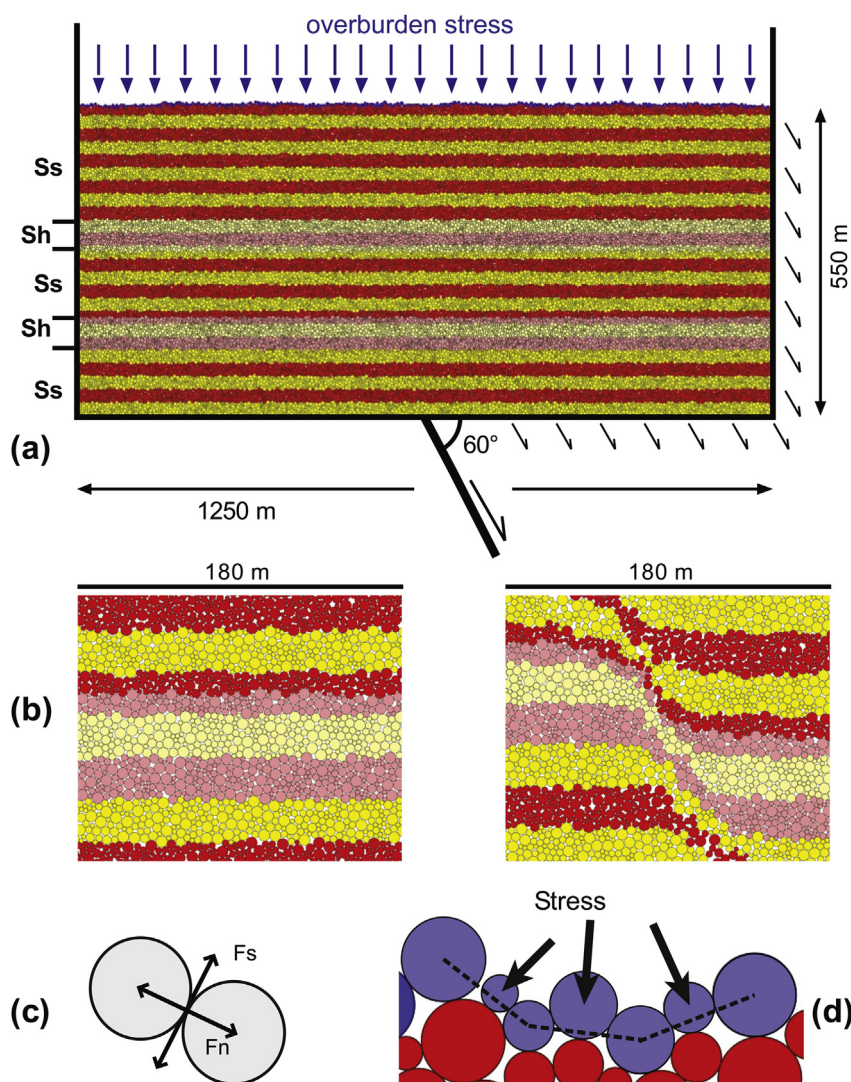


Figure 2. Example of the DEM used in the workflow: (a) Initial fault model with four different particle radii, sedimentary layering (Ss = sandstone and Sh = shale), and boundary conditions for a 60° dipping normal fault represented by the small black arrows on the hanging wall side of the model. (b) Zoom in before (left) and after (right) faulting. (c) Normal (Fn) and shear (Fs) forces at particle contacts. (d) Overburden stress applied normal to the top surface at the center of each particle.

For simulations at several kilometers depth in an upper crust full of discontinuities and in frictional equilibrium, a purely frictional failure envelope is a good representation of rock behavior (Hubbert, 1951; Zoback, 2010). In this case, the particle elasticity/stiffness chosen allows some overlap between the particles in contact (<1% of the particles combined radii), and thus frictional interaction without unrealistic overlaps.

Although the DEM is a mechanical model, it has some interesting similarities with analogue, scaled models. As in analogue models, the modeling materials should be chosen to reproduce the appropriate bulk rock behavior at the scale of consideration, so in the DEM the right particle properties should be chosen to give a realistic bulk rock behavior at the scale of the problem. In addition, just as in analogue models the grains of the modeling material are not the same as the grains of the rocks being modeled, so in the DEM the particles in the model do not represent the sedimentary rock grains. At the scale of our problem (a large fault), the DEM captures the bulk behavior and geometry of faulting and its associated deformation, but not the physical and chemical processes occurring at the grain scale. Even though the DEM does not target grain scale or rock-fluid interaction processes, it results in realistic fault development and evolution that we can use as input to our workflow. Many studies have shown the ability of the technique to reproduce realistic fault geometries in extensional and contractional settings, at seismic to sub-seismic scales and at reservoir depths (e.g. Egholm et al., 2008; Hardy et al., 2009; Hardy, 2011).

2.2. Change of seismic properties due to finite strain

Large displacement faults involve large and permanent deformations (folding and fracturing). Under this situation, we cannot easily relate stress to strain. Neither can we use standard, continuum rock physics equations to predict the change of elastic properties due to large finite strains. Few studies discuss the impact of large strains on rock properties. Holt et al. (2008) study the impact of small volumetric strains (lower than 1%) on seismic velocities in cm-scale sandstone and shale samples, Sigernes (2004) measured seismic velocities in cm-scale samples at several distances from the fault core in five normal fault outcrops in siliciclastic rocks. Skurveit et al. (2013) investigate deformation mechanisms and their impact on ultrasonic velocity during shear-enhanced compaction in poorly lithified sandstone. Hatchell and Bourne (2005) look at the impact of pressure depletion induced strain and fracturing on seismic velocities in a reservoir at a field scale. Although these studies encompass a large range of lithologies, scales and finite strain magnitudes, they broadly illustrate how volumetric strain and fracturing modify seismic velocities: compaction (i.e., negative volumetric strain) decreases porosity, thereby increasing density and seismic velocities, while dilation (i.e., positive volumetric strain) and shear or tensile induced fracturing have the opposite effect. Scaling of the lab results and outcrop studies to the larger dimensions and much lower wave frequencies of industry standard seismic is complicated, such that we do not know exactly how finite strain modifies acoustic properties at the reservoir scale.

We use the general consensus of the studies above. As a first hypothesis, we consider only the volumetric strain effects on seismic properties. Shear strain effects are of course important, particularly for fracture-induced porosity in low-porosity sedimentary rocks. Porosity, density, and seismic velocities are assigned to the rock materials in the DEM model before faulting (Fig. 2a). These values are averages from the literature adapted to the scale, depth and stress conditions of the simulations. In the models of Section 3, they correspond to sandstone (Hoek and Brown, 1997; Mavko et al., 2009) and shale (Horsrud et al., 1998; Nygård et al., 2006). At any stage of the DEM simulation, incremental and total

particle displacements are known. These are used to compute incremental or total strains (the gradients of the particles incremental or total displacements). We use a nearest-neighbor routine (Cardozo and Allmendinger, 2009) to compute strain. Essentially, we divide the DEM model into regular cells. At the center of each of these cells, the strain is computed from the displacements of the particles within a maximum radius from the cell center. We use a cell size appropriate for capturing the complexity of fault related strain, and a maximum radius large enough to include six particles in the strain computation (in 2D, a minimum of 3 particles are needed to compute strain; Allmendinger et al., 2012). Underlying the strain computation is the assumption that finite strain is homogeneous in the cells, thus we are converting (and in a way upscaling) the heterogeneous strain in the fault volume, to a cell-based strain. Although not a direct measure of the physical processes occurring in the rocks at the grain scale, the computed strain is a proxy for these processes (just as in a triaxial test, the axial strain of a sample is a proxy for the processes occurring in the sample at the grain scale). We use the computed finite strain and specifically dilatation (the product of the principal stretches minus one) to modify the initial rock properties. Data from Sigernes (2004) on siliciclastic and from Jeanne et al. (2012) on carbonate fault zones reveal highly variable density and P-wave velocity changes (e.g., from 10% to 50% and more) across and away from the faults. We assume here that the maximum changes of porosity, P-wave and S-wave velocities at our model scale are within a reasonable range of $\pm 25\%$ from their initial values due to dilation or compaction. The fact that 100% compaction is unrealistic is also taken into account (Fig. 3).

We modify the porosity from its initial value according to a linear relation (Fig. 3):

$$\phi = \phi_{ini}(0.25\varepsilon_v + 1), \quad -1 \leq \varepsilon_v \leq 1 \quad (1)$$

where ϕ is porosity, ϕ_{ini} is initial porosity and ε_v is volumetric strain. Rock density ρ is computed from porosity assuming saturated conditions:

$$\rho = \rho_g(1 - \phi) + \rho_w\phi \quad (2)$$

where ρ_g and ρ_w are grain and fluid densities respectively. P-wave velocity V_p follows a sigmoidal relation (Equation (3) and Fig. 3):

$$V_p = \begin{cases} V_{p_{ini}}(-0.25\varepsilon_v^2 - 0.5\varepsilon_v + 1), & -1 \leq \varepsilon_v < 0 \quad (\text{compaction}) \\ V_{p_{ini}}(0.25\varepsilon_v^2 - 0.5\varepsilon_v + 1), & 0 \leq \varepsilon_v \leq 1 \quad (\text{dilation}) \end{cases} \quad (3)$$

where $V_{p_{ini}}$ is the initial P-wave velocity. This sigmoidal relation emphasizes that the change of V_p is more significant at lower strains than at relatively large strains. For sandstone and shale, the relation between V_p and S-wave velocity V_s is within the range defined by Han's and Castagna's empirical laws (Sigernes, 2004). We use the Han's relation to compute V_s :

$$V_s = 0.794V_p - 0.787 \quad (4)$$

Equations 1–4 allow us to compute the change of seismic properties due to finite volumetric strains. Even if the estimated values are not accurate, they are within a reasonable range (for poorly lithified sediments, the changes of acoustic properties due to large volumetric strains can be more dramatic; Skurveit et al., 2013 and Fig. 3). Relative changes of seismic properties within the fault zone rather than their absolute values are more important for seismic imaging.

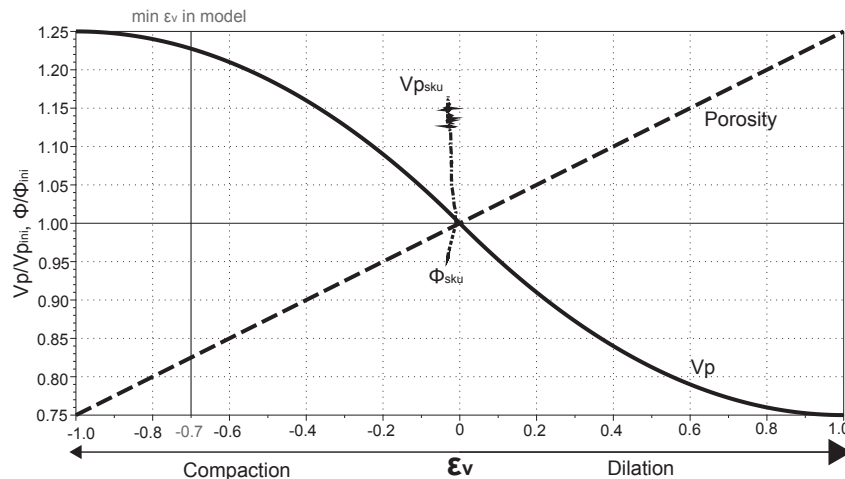


Figure 3. Assumed change of porosity ϕ and P-wave velocity V_p with volumetric strain ϵ_v . ϕ_{ini} and $V_{p,ini}$ are porosity and P-wave velocity before faulting. ϕ_{sku} and $V_{p,sku}$ are porosity and P-wave velocity from triaxial testing of poorly lithified sandstone at 15 MPa (Skurveit et al., 2013).

2.3. Simulated seismic imaging

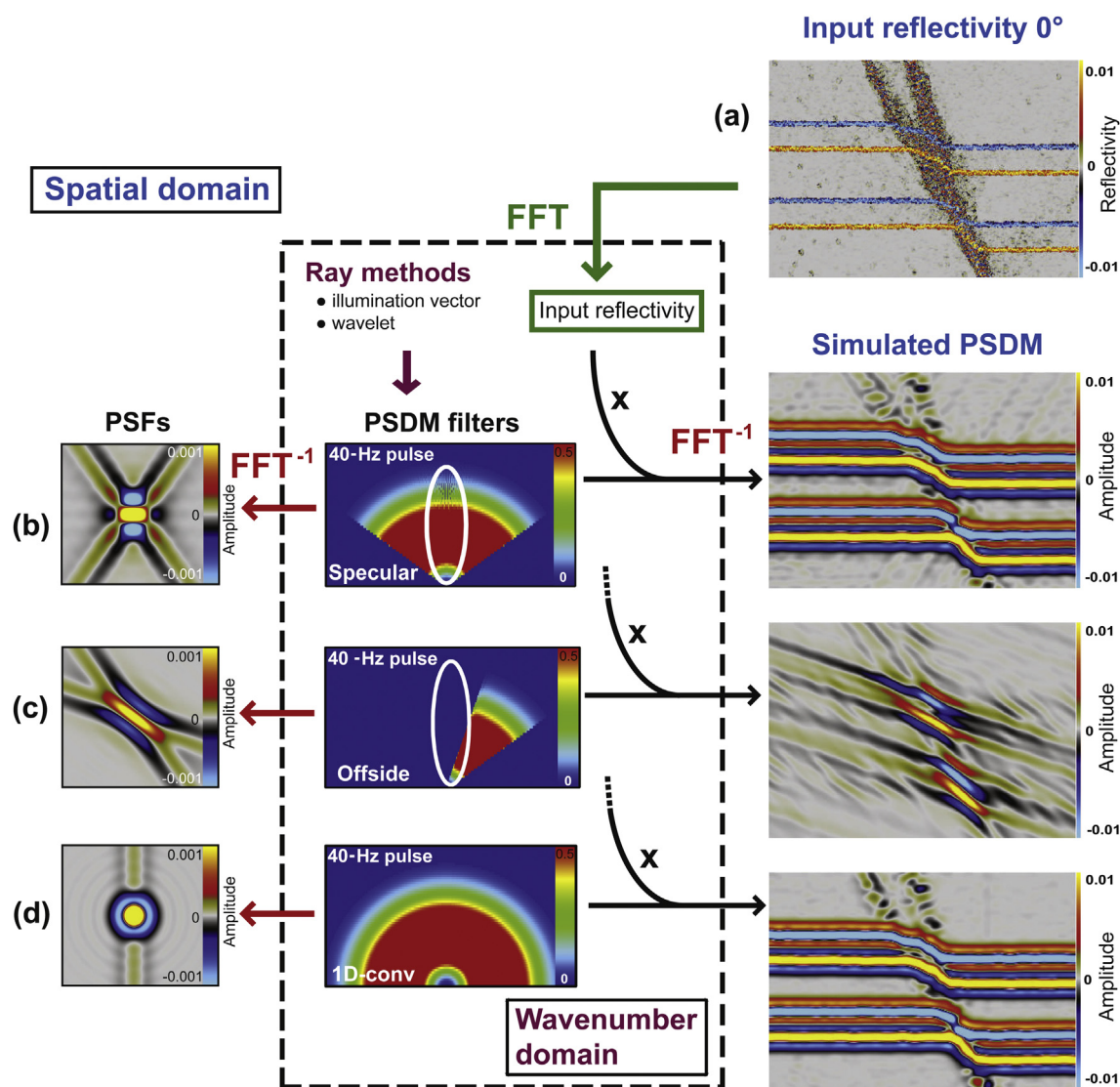
Seismic imaging simulation is used to assess the impact of fault internal structure and properties on the resulting seismic image. With the known architecture and estimated rock properties of the fault from geomechanical modeling, it is possible to experiment with various parameters (especially those related to survey design, but also processing) to see their impact on the seismic images. The technique we use is a 3D PSDM simulator (Lecomte, 2008). This simulator acts as an image-processing method by distorting the input reflectivity to reproduce the effects of seismic imaging in PSDM mode.

The standard trace-modeling method of the industry is 1D convolution in the time domain, i.e., convolution of a vertical reflectivity log in time with a wavelet. 1D convolution can only simulate poststack time-migrated sections for limited and non-totally realistic modeling cases, i.e., for full-aperture surveys and models without lateral variations (1D). Applying 1D convolution to 2D/3D models can be misleading, with possible mis-positioning of seismic events and total lack of lateral resolution effects. To the contrary, the PSDM simulator (Lecomte, 2008) works in the pre-stack domain and in depth, and properly handles 3D effects in resolution and illumination as function of various parameters such as velocity model, survey geometry, wavelet, etc. (Lecomte and Kaschwich, 2008). Besides vertical resolution, which is more or less predicted by 1D convolution, the PSDM simulator reproduces also lateral resolution effects such as those resulting from faults or other structural discontinuities. Another important feature of this seismic modeling approach is the automatic integration of 3D illumination effects, i.e., the ability of the simulator to properly reproduce whether or not a given structure will be seen by seismic. Though largely going beyond the limitations of 1D convolution, the PSDM simulator is still approximate in comparison to direct modeling methods solving the full-wave equation (e.g., via finite differences – FD), because it does not take into account the complete wavefield and considers only single scattering. The processing time of the PSDM simulator is however quite similar to 1D convolution, because PSDM cubes are generated directly from input reflectivity cubes, i.e., without calculating synthetic recordings and processing them, as it would be done in a standard FD-based modeling followed by PSDM. The latter approach is far more complex and time-consuming, requiring several codes and expert users. The PSDM simulator is therefore still a fast and robust

approach, more advanced than 1D convolution, and allowing efficient and near-interactive sensitivity analyses on various seismic parameters (Drottning et al., 2009).

The structural input to the PSDM simulator is an angle-dependent reflectivity cube, which is obtained from the acoustic properties of the model, i.e., density, V_p and V_s (Fig. 4a). This reflectivity cube can be converted to the wavenumber domain using a Fast Fourier Transform (FFT, Fig. 4a), and further processed using ray-based modeling to build the so-called PSDM filters. For these, and key to the method, illumination vectors (Lecomte, 2008) are calculated at a given reference point (e.g., center of the target) using ray-based methods (Gjøystdal et al., 2007). The illumination vectors are computed according to a selected survey, wave type, velocity model and other PSDM related parameters. They are formed at the considered point as a combination of the incident ray and the scattered one. In case of specular reflection (i.e., following Snell's law), the illumination vectors direction indicate which reflector dips will be seen by the seismic waves, i.e., the reflectors normal to the illuminations vectors. But the illumination vectors are also indicative of other scattering patterns and therefore cover diffraction effects too, as demonstrated by Kaschwich et al. (2011). From the illumination vectors and a given wavelet, a PSDM filter is generated in the wavenumber domain (Fig. 4b–c, center). Figure 4b (center) is the PSDM filter corresponding to a complete survey acquisition with illumination of a wide range of dips, including the horizontal ones (the latter corresponds to the vertical band in the PSDM filter). Figure 4c (center) is the PSDM filter using a sub-selection of the survey to generate an off-side illumination, chosen to avoid illuminating the flat reflectors (the vertical band in the PSDM filter is not covered). Figure 4d (center) is an ideal (synthetic) case where all reflector dips would be illuminated; no survey can really produce such cases in practice. This latter case is somewhere similar to 1D convolution.

Finally, the PSDM filter is applied to the input reflectivity in the wavenumber domain, and an FFT^{-1} over this result is used to produce the simulated PSDM cube in the spatial domain (Fig. 4b–c, right). Note that the application of an inverse FFT (FFT^{-1}) to the PSDM filter itself yields the corresponding Point-Spread Function (PSF) in the spatial domain, that is the image response of a point scatterer at the reference point (Fig. 4b–c, left; Lecomte, 2008). Such PSF is indicative of the local imaging capability of the PSDM, i.e., how well retrieved a point scatterer will be, which is especially important for features such as faults, fractures, and other structural



discontinuities. Applying the PSDM filter to the input reflectivity in the wavenumber domain is equivalent to a 3D convolution of the PSF with the reflectivity cube in the spatial domain. The process in the wavenumber domain is however more efficient when using only one PSF for the whole target model, as done here, as we only consider one reference point (center of the images). Spatially variable PSFs can also be applied for a more accurate imaging, depending on the size of the target zone (here fault zones), although this is more time-consuming. Preliminary results of spatially-variable PSF modeling can be found in [Zühlsdorff et al. \(2013\)](#), and are more relevant when dealing with 3D models.

The resulting simulated PSDM cubes are more realistic than the image produced by 1D convolution considering the limitations of the latter, especially its lack of model-based wave-propagation effects for a given survey. 1D convolution can only be realistic for geological structure of low complexity (weak lateral velocity variation). As an approximation to 1D convolution, the PSDM simulator was used with a perfect PSDM filter, i.e., with illumination of all

reflector dips, but still with a certain width due to the frequency band of the wavelet (Fig. 4d, center). This corresponds in the spatial domain to a more point-wise PSF whose size only depends on the wavelength frequency band and the velocity at the reference point (Fig. 4d, left). A true 1D-convolution operator would even be narrower laterally, i.e., corresponding to a 1D (vertical) PSF. Though the obtained image (Fig. 4d, right) resembles the other PSDM-simulated ones (Fig. 4b, c, right), except for less migration noise in Figure 4d, there is no way to experiment with other parameters than the frequency band (vertical resolution), and certainly no possibility to consider realistic geologic models and surveys with correct lateral resolution and illumination effects.

3. Application: large normal fault

We show the application of the workflow in 2D to a 60° dipping normal fault in a 1.25 × 0.55 km interbedded sandstone-shale sequence (Fig. 2a). The fault is imposed as a displacement

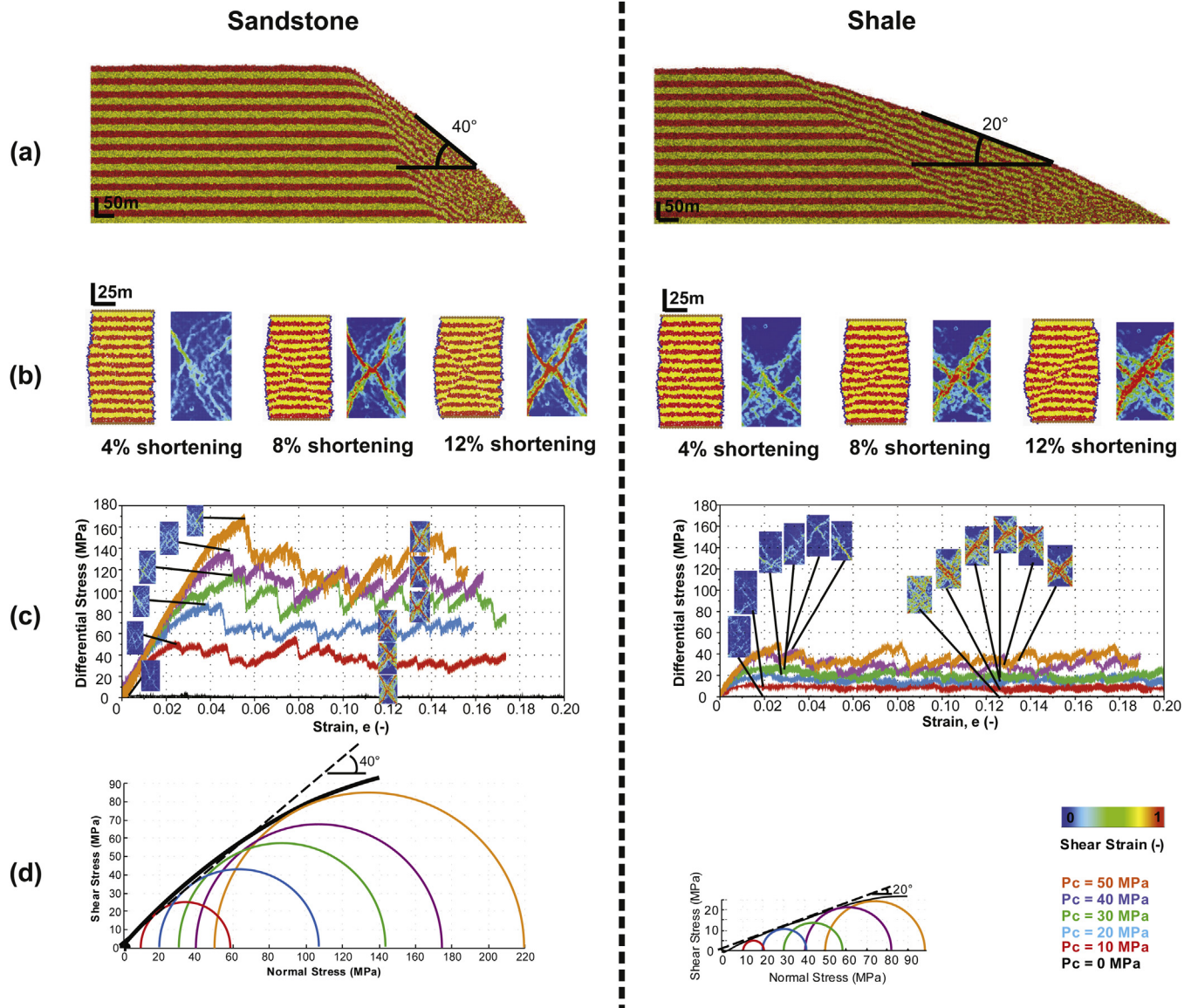


Figure 5. Bulk response of the coarse sandstone and shale assemblages for the input particle properties of Table 1. (a) Collapse simulations. (b) Biaxial compressive simulations under 20 MPa confining pressure at three shortening stages (left is geometry and right is shear strain). (c) Axial strain vs. differential stress curves. Rectangular images are samples colored by shear strain at different values of axial strain. (d) Failure envelopes from biaxial simulations.

boundary condition at the base of the model (Fig. 2a). The shale layers are 50 m thick and are thinner and more incompetent than the sandstone layers (Fig. 2a). The competence contrast between the shale and the sandstone layers has significant impact in both the DEM and the simulated seismic images. A normal stress of 25 MPa is applied at the top of the model, representing a sedimentary overburden of about 1.5 km (Fig. 2a). To investigate the impact of particle size on fault evolution, two DEM assemblages of similar bulk stress–strain behavior are considered. The first assemblage is constituted of 45,000 particles with four different radii going from 1.25 to 3.125 m. We refer to this assemblage as the “coarse model”. The second assemblage has 180,000 particles with four different radii going from 0.625 to 1.5625 m. We refer to this assemblage as the “fine model”. These two, 2D models are used to illustrate the impact of faulting on seismic properties, and to run sensitivity analyses of the effect of illumination direction and frequency on the resulting seismic images.

3.1. Mechanical modeling

3.1.1. Coarse model

3.1.1.1. Material calibration. As discussed in Section 2.1, the first step in the DEM simulation is to calibrate the assemblage so that it mechanically behaves like a real rock, in our case sandstone and shale, at the scale and depth of consideration. To do this, we use two tests: 1. Collapse simulations at km scale where initially the assemblage is inside a rigid box, and then one side of the box is removed, allowing the measure of the static angle of repose of the material (Fig. 5a); and 2. Biaxial compression simulations at different confining pressures, which allow determining the failure envelope of the material (Fig. 5b and c). The dimensions of the biaxial samples are 125 × 250 m (Fig. 5b), which is a representative size of the DEM simulation (Fig. 2a–b), but does not target laboratory (cm) to grain (mm) scales.

For the four particle radii going from 1.25 to 3.125 m and for the particle properties of Table 1 (particles density, stiffness and

Table 1

Particle properties of the coarse and fine assemblages for sandstone and shale materials.

Input parameters:		4 particle radii (m)	Density of particles (kg/m ³)	Particle stiffness (GPa)	Particle friction
Sandstone	Coarse	1.25–3.125	2500	5.6	0.35
	Fine	0.625–1.5625			
Shale	Coarse	1.25–3.125	2500	5.6	0.1
	Fine	0.625–1.5625			

interparticle friction), the bulk response of the assemblages representing sandstone and shale is summarized in Figure 5 and Table 2. The interparticle friction is the main parameter controlling the competence of the material. The interparticle friction in the shale is about one third that in the sandstone (Table 1), such that the bulk internal friction angle (ϕ_i) of the shale is about half that of the sandstone in both, the collapse simulations (Fig. 5a) and the biaxial tests (Fig. 5b–c, Table 2). Sandstone and shale are known to have a large range of values of mechanical properties. For reservoir conditions at the depth of our study, an internal angle of friction of 40° (Fig. 5a) is adequate for consolidated sandstone (Zoback, 2010). A bulk internal friction angle of about 20° (Fig. 5b) is consistent with North Sea shale at 1–2 km depth (Horsrud et al., 1998). Notice that even though the mechanical behavior of the sandstone and shale assemblages is purely frictional (zero strength at zero confining pressure and no tensile strength), there is strain localization (i.e., faulting) in both the sandstone and shale, as indicated by the shear strain of the samples at different amounts of shortening (Fig. 5b–c). The sandstone presents two conjugate faults, each one making an angle of about 25° ($45^\circ - \phi_i/2$) with the direction of the axial stress (σ_1). The shale shows two conjugate faults, less localized than in the sandstone, and making an angle of about 35° with σ_1 . In the sandstone and shale, the expected normal fault dip angles ($45^\circ + \phi_i/2$) are 65 and 55°, respectively. The fault displacement boundary condition at the base of the DEM model, corresponding to a 60° dipping normal fault (Fig. 2a), is consistent with the mechanical behavior of the sandstone and shale materials.

3.1.1.2. Evolution of geometry and finite strain. To model the 60° dipping fault, we use the DEM model presented in Figure 2a, with extension of the model controlled by the displacement of the assemblage boundary particles of the hanging wall parallel to the dip direction. The model was run to 100 m fault displacement with a total horizontal extension of 50 m. Figure 6 presents the evolution of the model geometry (left), shear strain (center), and volumetric strain (right) at four stages of vertical fault displacement: 10, 40, 60 and 100 m (Fig. 6a–d). At 10 m fault displacement (Fig. 6a), a fault starts to propagate across the assemblage. The fault dips steeply, about 65°–70° in the sandstones, and at a lower angle of about 60° in the shale. A second less steep fault nucleates from the initial fault in the center sandstone layer around 40 m fault displacement

(Fig. 6b). The dip angle of this second fault in the sandstone and shale layers is 60° and 50°, respectively. These two faults continue to develop until later stages (Fig. 6b–d). From 80 m fault displacement, the second, less steep fault becomes more active displaying larger displacements and shear strains (Fig. 6d). From 60 m fault displacement, there are visible offsets of the sandstone layers, especially the top layer, while the shale layers are smeared across the fault zone (Fig. 6c–d, left). Shear strain (Fig. 6, center) shows that the evolution of the normal fault zone is complex with low and narrow strain areas at early development (Fig. 6a–b), to high and broader (e.g., up to 50 m) strain areas at large displacements (Fig. 6c–d). High shear strain zones link to form larger faults. At 10 m fault displacement (Fig. 6a), the fault segments have already linked to form the main fault. The second fault starts to develop at about 20 m fault displacement and links to the first one at about 40 m fault displacement (Fig. 6b). Volumetric strain increases with fault displacement, mainly with a dilation component (positive volumetric strain, red in the web version, Fig. 6 right), although at certain locations the fault is under compaction (negative volumetric strain, blue, Fig. 6 right). The highest shear strain regions correlate with the highest dilation and compaction. The shale layers experience higher compaction and thinning within the fault zone, especially the lowest shale layer (Fig. 6, right). At 100 m fault displacement, the more incompetent shale layers show continuous smearing across the two faults, whereas the sandstone, including the center layer, display clear, different offsets across the two faults (Fig. 6d, right).

3.1.1.3. Change of seismic properties. Seismic imaging simulation needs an input reflectivity model of the fault at a given amount of displacement. Seismic resolution of the fault will be dependent on the amount of fault displacement. To have a sufficient impact on the displacement of the reflectors and on the resultant seismic image, we choose to use the normal fault DEM model at 60 m of fault displacement (Fig. 6c). At this amount of fault displacement, the shale layers are not completely offset, but the fault structure is sufficiently complex to investigate on seismic. To compute the seismic properties in the fault, we assign elastic properties to the sandstone and shale before faulting (Table 3). These properties are average values from the literature for intact sandstone (Hoek and Brown, 1997; Mavko et al., 2009) and shale (Horsrud et al., 1998; Nygård et al., 2006) at ~1.5 km depth and at the scale of the DEM. The computed finite volumetric strain (section 2.2) at 60 m of fault displacement (Fig. 6c right) is then used to modify the initial rock properties (Table 3) using Equations 1–4. Figure 7 shows the change of density (Fig. 7a) and seismic velocities (Fig. 7b) at 60 m of fault displacement. As expected from the mechanical properties of the sandstone and shale (Fig. 5), the shale layers within the fault zone experience more volumetric strain and larger relative changes in wave velocities and density than the sandstone layers.

3.1.2. Fine model

To investigate the impact of particle size on the DEM simulation and its resultant seismic images, we use a normal fault model as in Figure 2a, but with half-sized and four-times more particles than in the coarse model of the previous section.

3.1.2.1. Material calibration. With the exception of particle radii, particle properties in the fine sandstone and shale assemblages are the same as in the coarse assemblages (Table 1). However, smaller particles in the fine assemblage require a smaller time step of computation, resulting in significant longer runtimes. Due to this time and computing limitations, only biaxial compression simulations at different confining pressures were run for the calibration of the fine sandstone and shale assemblages (Fig. 8). As in the biaxial

Table 2

Calibration results for the coarse and fine, sandstone and shale assemblages. The angles of repose and internal friction are equivalent.

Calibration results:		Angle of repose	Angle of internal friction	Coefficient of internal friction	Fault dip in extension
Sandstone	Coarse	40°	40°	0.84	65°
	Fine	↘			
Shale	Coarse	20°	19°	0.36	55°
	Fine	↘			

↘ This back slash means that there is no value available for this box.

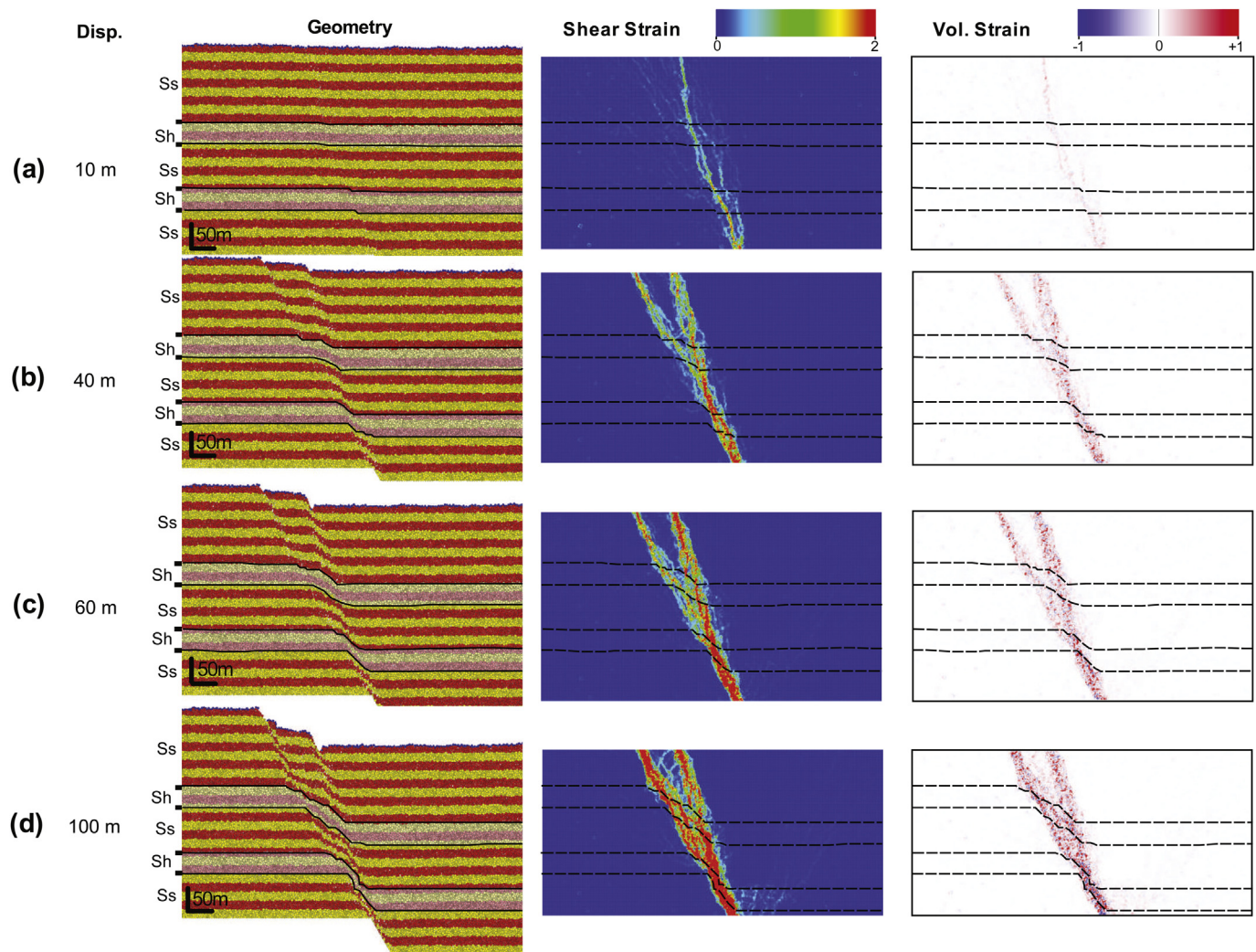


Figure 6. Evolution of the coarse DEM normal fault simulation at: (a) 10, (b) 40, (c) 60 and (d) 100 m of fault displacement. Left is geometry, center is shear strain, and right is volumetric strain. Ss and Sh represent sandstone and shale layers respectively. Black lines are layer boundaries.

tests for the coarse assemblages, the dimensions of the samples for biaxial compression of the fine assemblages are 125×250 m (Fig. 8a). For the four particle radii going from 0.625 to 1.5625 m and for the particle properties of Table 1, the bulk stress–strain response of the fine sandstone and shale assemblages is close to that of the coarse ones (Figs. 8 and 5 and Table 3). Biaxial simulations of the fine sandstone and shale assemblages under a confining pressure of 20 MPa (Fig. 8a), show an evolution of faulting similar to the one observed in the biaxial tests of the coarse sandstone and shale assemblages at the same confining pressure (Fig. 5b). Faulting in the fine and coarse sandstone and shale assemblages is also similar at other confining pressures between 0 and 50 MPa (Figs. 8b and 5c). However, in the fine sandstone and shale assemblages, there is more strain localization and the fault zones are narrower and better defined (Fig. 8a). Stress–strain curves and failure envelopes of the fine and coarse sandstone and shale assemblages are

Table 3
Acoustic properties assumed for the unfaulted sandstone and shale materials.

	Φ_{ini}	ρ_g (kg/m ³)	$\rho_{tot\ ini}$ (kg/m ³)	$V_P\ ini$ (km/s)	$V_S\ ini$ (km/s)
Sandstone	0.15	2650	2402.5	4	2.389
Shale	0.3	2700	2190	2	0.801

similar, although the stress–strain curves of the coarse assemblages display more variability (Figs. 8b and 5c). For similar particle properties and bulk stress–strain behavior, particle size influences strain localization, extent of faulting and its resolution. Although the fine and coarse sandstone and shale assemblages have similar bulk mechanical behavior, they are essentially different. The fine sandstone and shale assemblages result in narrow fault zones, while the coarse assemblages give more distributed fault related deformation. This numerical issue can to some extent reflect what is observed in nature, where faulting in rocks of similar bulk mechanical behavior may be expressed as either narrower or broader zones of fault related deformation.

3.1.2.2. Evolution of geometry and finite strain. A normal fault DEM simulation with dimensions and boundary conditions similar to Figure 2a was run in the fine assemblage. The number of particles in this DEM model is 180,000. Figure 9 shows the evolution of the model geometry (left), shear strain (center), and volumetric strain (right) at 20, 40, 60 and 90 m of fault displacement (Fig. 9a–d). Fault evolution is different than that of the coarse model. At early stages (up to 20 m of fault displacement, Fig. 9a), the fault consists of several narrow segments. Each of these segments is up to 10 m and displays high shear and volumetric strain (Fig. 9a center and

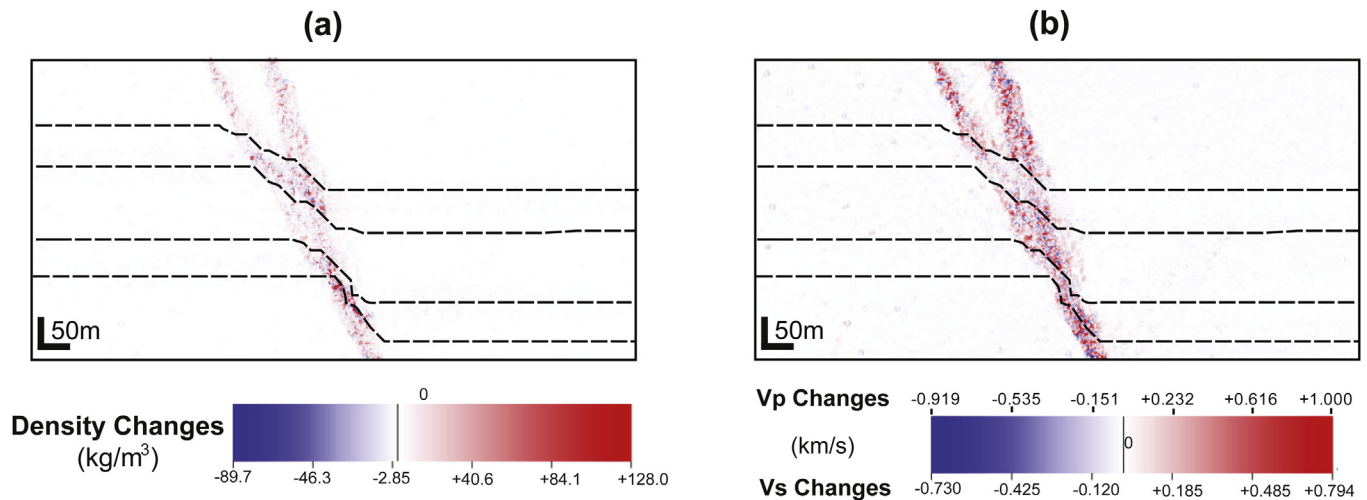


Figure 7. Changes of (a) Density and (b) Seismic velocities in the coarse model after 60 m of fault displacement. Black dashed lines are layer boundaries. Changes in the shale layers are more pronounced due to larger volumetric strains.

right). These fault segments dip 65° in the sandstone and $55\text{--}60^\circ$ in the shale. At 40 m of fault displacement, the fault segments are larger and have accumulated more strain, but they have not totally linked yet into a through going fault (Fig. 9b). Only at about 60 m of fault displacement, the fault segments are fully linked into a main fault with a throw of about 50 m (Fig. 9c). From 50 m of fault displacement, a less steep fault in the footwall of the main fault develops (Fig. 9b, center). This second fault also consists of several fault segments displaying high strain. These fault segments dip 60° in the sandstone and $40\text{--}45^\circ$ in the shale (Fig. 9c–d). From 60 m of fault displacement, smaller synthetic and antithetic normal faults develop linking the two major faults, especially in the center sandstone layer, but also in the top shale layer (Fig. 9c–d). The highest strains are localized in the major largest fault, and the shale layers accumulate more volumetric strain (Fig. 9d, center and right). The extent of fault related deformation (i.e. width of fault zone) is less than in the coarse model (Figs. 9 and 6). At early stages, the fault is mainly subjected to dilation (in red in the web version Fig. 9a, right), while at later stages both compaction and dilation occur along the two main faults, with the highest volumetric strains corresponding to the highest shear strains (Fig. 9b–d, right). The resolution of the fine model is higher than that of the coarse model, allowing capturing more details of fault formation, e.g. where the fault segments connect, as well as minor synthetic and antithetic faults that link the two major faults. Smaller particles give narrower fault zones. The particle size can also be responsible for the difference in fault dip angles between the two DEM models, but these differences can also be due to slight variations in the bulk properties of the assemblages.

3.1.2.3. Change of seismic properties. As in the coarse model, we choose the fine normal fault model at 60 m of fault displacement (Fig. 9c) to compute the change of elastic properties due to faulting. The same initial rock properties for sandstone and shale (Table 3) are assigned to the unfaulted fine model. Equations 1–4 are used to modify the initial elastic properties using the computed finite volumetric strain. Figure 10 shows the changes in density (Fig. 10a) and seismic velocities (Fig. 10b) in the fine model at 60 m of fault displacement. Since the shale layers accrued more volumetric strains, these layers exhibit the highest relative changes of elastic properties (Fig. 10). The lateral extent of faulting is less than in the

coarse model (Figs. 10 and 7), which results in less impact of the fault zone on its seismic image (section 3.2).

3.2. Simulated seismic imaging

For both the coarse and fine models, the values of density and seismic velocities after 60 m of normal fault displacement (Figs. 7 and 10) were used to compute the corresponding reflectivity grids with a 0° incident angle (Fig. 15a and b, first column). A few sensitivity studies were run to illustrate the impact of the fault on the resulting seismic images. The parameters explored here are the illumination direction (model and survey dependent in real cases) and the wave frequency. Comparison of seismic amplitudes and input elastic properties along interpreted reflectors was also performed, to assess the potential of the different seismic images for predicting fault architecture and internal properties.

3.2.1. Impact of illumination direction

The illumination direction has an impact on the total fault volume illuminated in the seismic image. The PSDM simulator was applied for a 1.5 km thick homogeneous overburden with a P-wave velocity of 4.0 m/s and shear wave velocity 2.389 m/s, zero-phase Ricker pulses of 10–40 Hz main frequency (a Ricker pulse is a special type of wavelet defined by its dominant frequency, and zero-phase means the wavelet is symmetrical with a maximum at time zero), and three different illumination directions (Figs. 11 and 12). The survey consists of a single streamer centered at the fault for the specular illumination, or offset towards the footwall or hanging wall for the left and right side illuminations, respectively.

Specular illumination (i.e., following Snell's law) is good for imaging reflectors; it corresponds to illumination vectors perpendicular to the reflectors, which in this case are horizontal outside the fault zone (the specular illumination is then vertical). If specular illumination exists, the corresponding reflectors dominate the seismic image, as in the case of the coarse normal fault model (Fig. 11, first column). However, some seismic energy related to diffractions from the fault is still visible especially at higher frequencies (Fig. 11, first column). The fault thus impacts the seismic image. The illuminations from the left or right sides, corresponding to different wave propagation directions, do not contain specular energy from the flat reflectors, but only diffracted energy from the fault (Fig. 11, second and third columns). The illumination from the

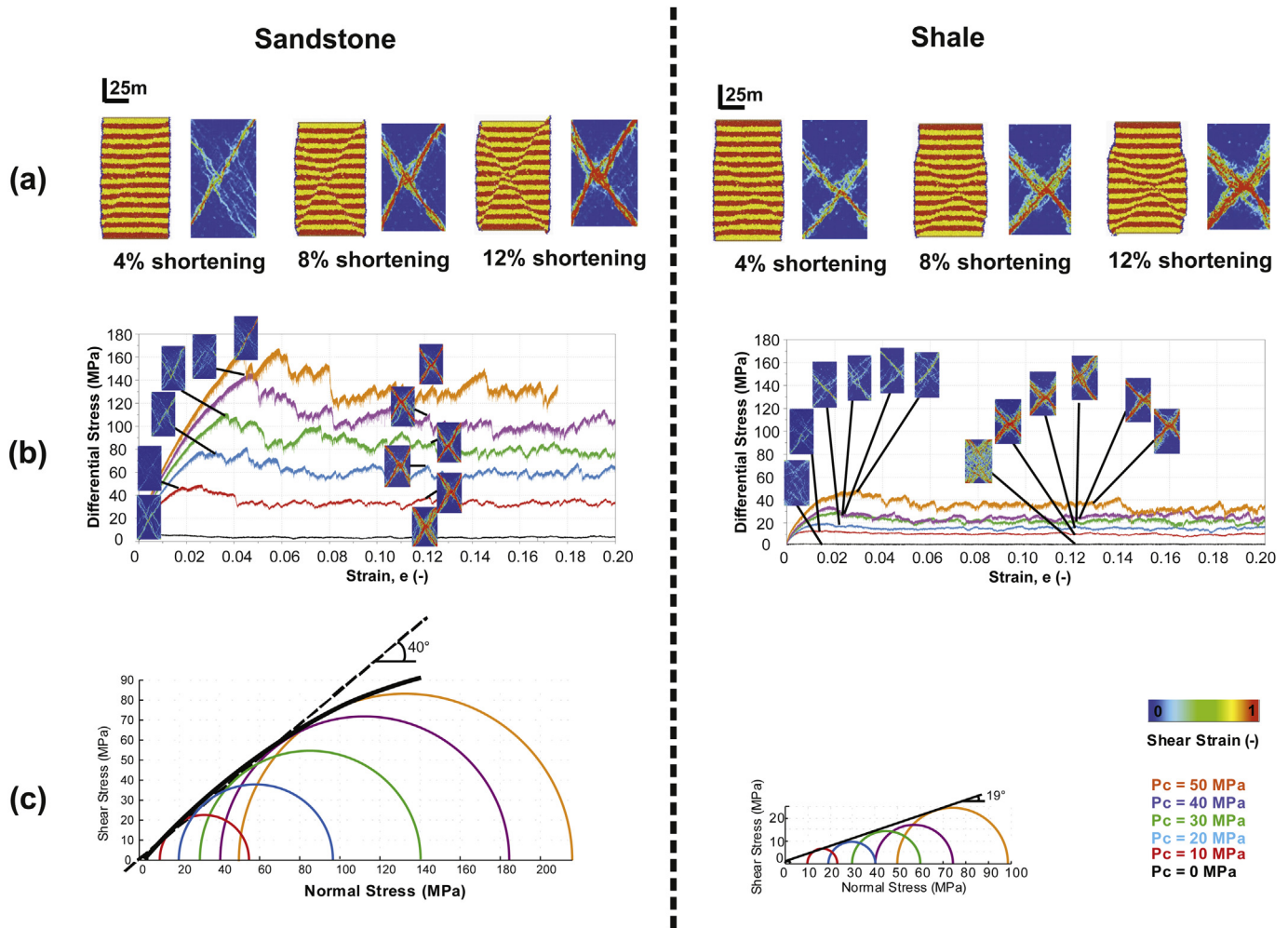


Figure 8. Bulk response of the fine sandstone and shale assemblages for the input particle properties of Table 1. (a) Biaxial compressive simulations under 20 MPa confining pressure at three shortening stages (left is geometry and right is shear strain). (b) Axial strain vs. differential stress curves. Rectangular images are samples colored by shear strain at different values of axial strain. (c) Failure envelopes from biaxial simulations.

footwall side (i.e., left side) produces an image with low amplitude values in which it is difficult to distinguish the two shale layers or to associate the reflections and diffractions to the fault structure. Higher amplitudes are visible at the top of the lower shale layer, which is offset (Fig. 11, second column). The illumination from the hanging wall side (i.e., right side), however, highlights the shale layers in the fault zone (particularly at frequencies of 20 Hz or more, Fig. 11, third column). These shale layers, which experienced higher finite strains than the sandstone layers (Figs. 6c and 7), are indicated by higher amplitude values. The changes in amplitude seem to correlate with the amount of finite strain, with lower amplitude values in the upper less deformed shale layer, and higher amplitude values in the lower more deformed one (Fig. 11, third column). For the left or right side illuminations, diffractions are related to the structural complexity of the fault zone (Fig. 11, right), but also to the irregular, jagged geometry of the shale/sandstone layer boundaries (Fig. 11, second and third columns).

Figure 12 shows the corresponding seismic images for the fine normal fault model. Even if the general aspect of the seismic images for the fine model (Fig. 12) is similar to those for the coarse model (Fig. 11), there are significant differences. In fact, using the coarse and fine models is an effective way to test the potential of seismic to differentiate between the fault related structure of these models (Figs. 6c and 9c). Specular illumination in the fine model highlights

mainly the shale layers and their folding without major diffractions associated to the two fault segments (Fig. 12, first column). The small offset of the top of the upper shale layer is visible by a decrease of the amplitude value. The smaller fault segment towards the footwall of the main fault is almost not noticeable, but just indicated by a gentle downward bending of the upper shale reflectors (Fig. 12, first column). Diffractions can be detected but are difficult to interpret. Diffractions associated to reflectivity changes within the fault zone have large impact on the resulting image. Although it is easy to delimit the offset of the main fault, it is difficult to tell that there is another smaller fault segment, even at high frequencies (Fig. 12, first column). Footwall illumination gives low amplitude images (Fig. 12, second column). However, some extra information can be extracted from these images. The folding of the shale layers associated to the main fault segment generates higher amplitude reflections, either by significant thinning of the layer (e.g. lower shale layer) or layer offset (e.g. top shale layer). The smaller fault segment in the top upper shale layer is marked by diffracted energy (Fig. 12, second column). Hanging wall illumination (Fig. 12, third column) illuminates directly the main fault plane and the steeply dipping shale layers within the fault zone. The smaller fault segment, however, is not distinguishable because its related diffractions interact with those of the main fault segment.

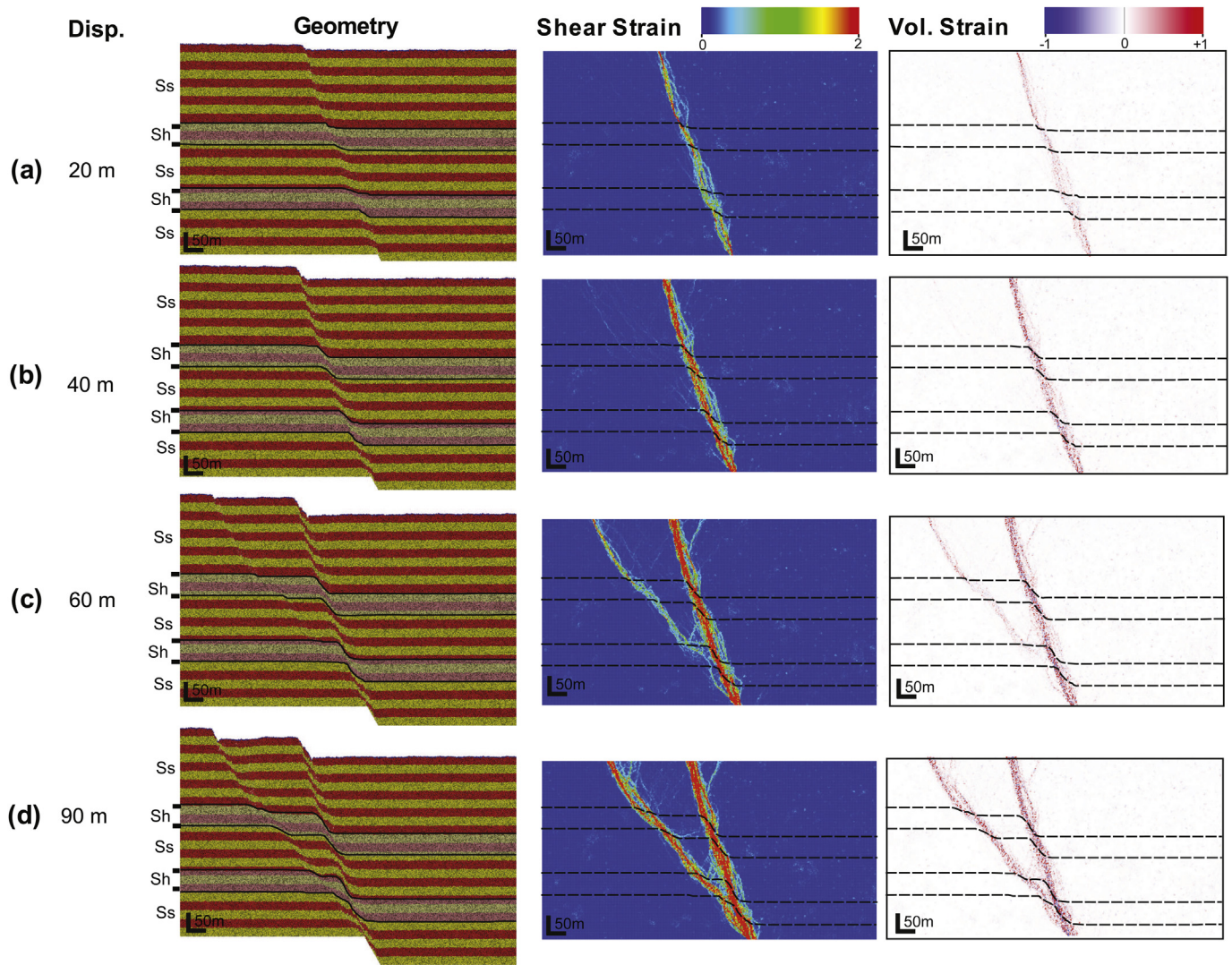


Figure 9. Evolution of the fine DEM normal fault simulation at: (a) 20, (b) 40, (c) 60 and (d) 90 m of fault displacement. Left is geometry, center is shear strain, and right is volumetric strain. Ss and Sh represent sandstone and shale layers respectively. Black lines are layer boundaries.

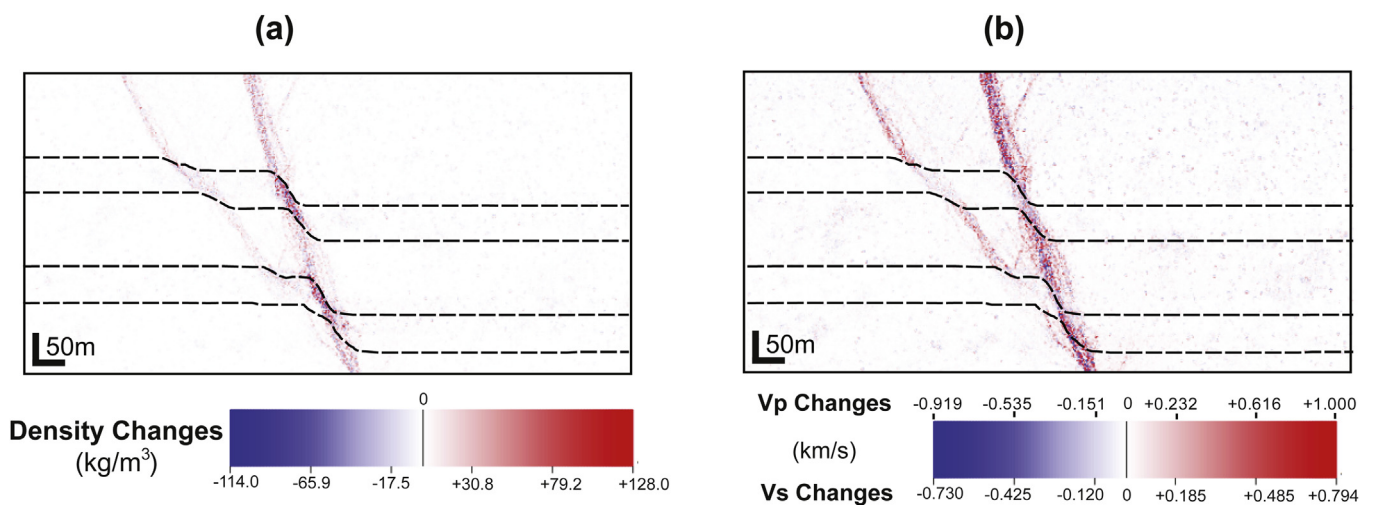


Figure 10. Changes of (a) Density and (b) Seismic velocities in the fine model after 60 m of fault displacement. Black dashed lines are layer boundaries. Changes in the shale layers are more pronounced due to larger volumetric strains. Density changes are more pronounced than in the coarse model (Fig. 7).

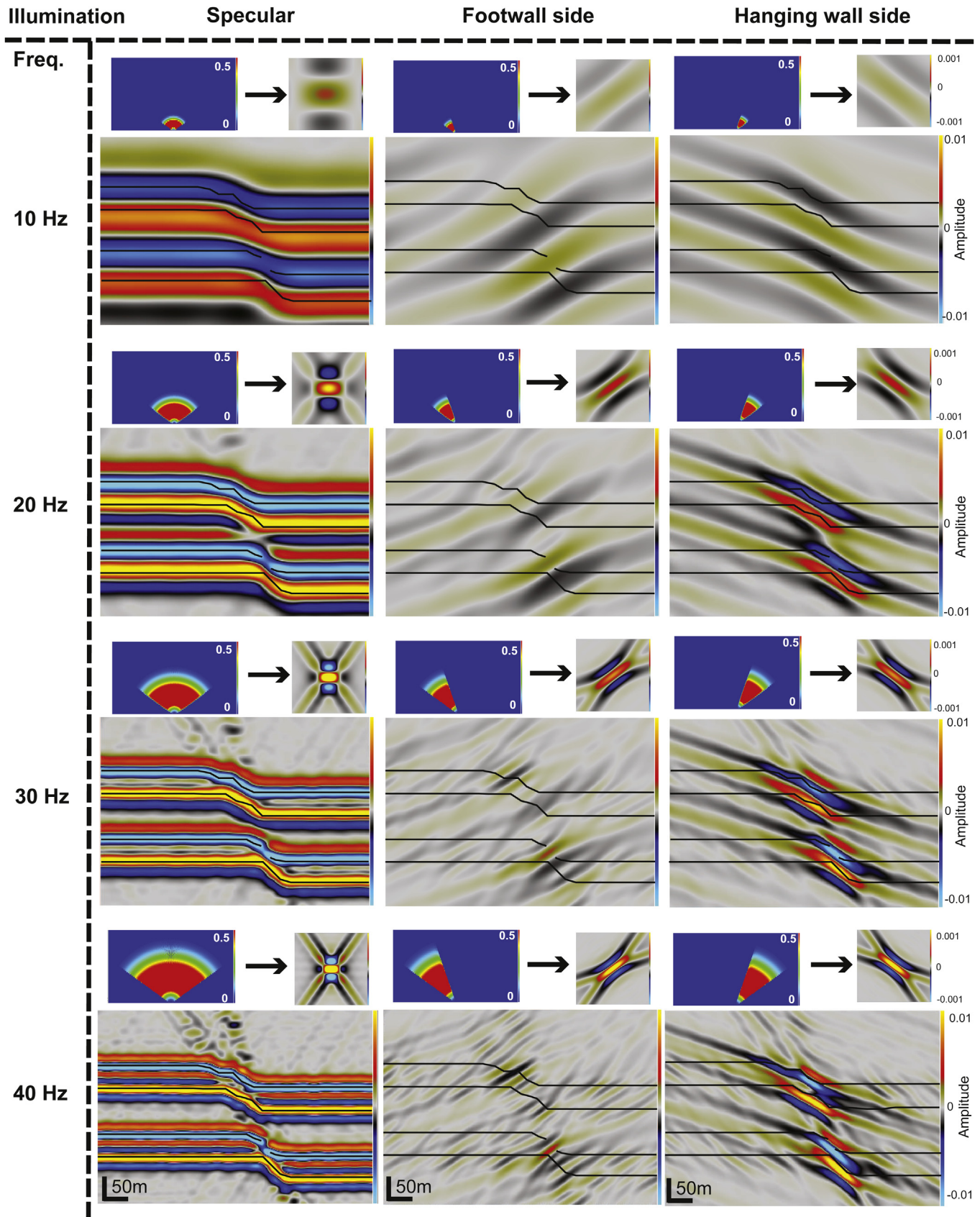


Figure 11. PSDM seismic images of normal fault coarse model at 60 m of fault displacement. The columns correspond to three different illumination directions: direct (left), footwall or left side (center), and hanging wall or right side (right). The rows correspond to four different frequencies of an incoming zero-phase Ricker pulse: 10 (first row), 20 (second row), 30 (third row), and 40 Hz (fourth row). At the top of each seismic image the PSDM filter and corresponding point spread function or PSF are shown. The overburden is 1.5 km and is homogeneous. Black lines are layer boundaries.

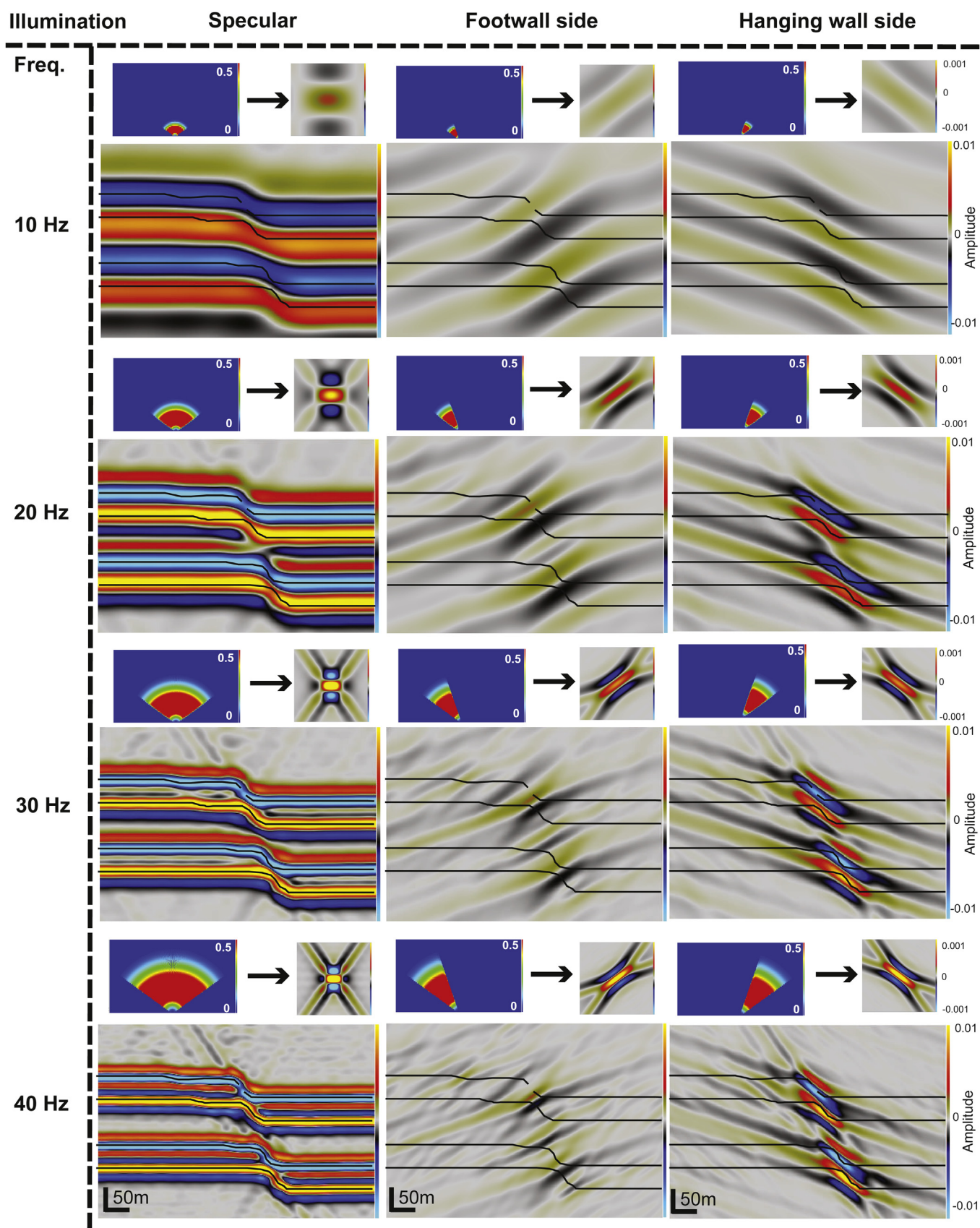


Figure 12. PSDM seismic images of normal fault fine model at 60 m of fault displacement. The columns correspond to three different illumination directions: direct (left), footwall or left side (center), and hanging wall or right side (right). The rows correspond to four different frequencies of an incoming zero-phase Ricker pulse: 10 (first row), 20 (second row), 30 (third row), and 40 Hz (fourth row). At the top of each seismic image the PSDM filter and corresponding point spread function or PSF are shown. The overburden is 1.5 km and is homogeneous. Black lines are layer boundaries.

3.2.2. Impact of frequency

Wave frequency is one of the parameter controlling the resolution of the fault in the resulting seismic image. In the coarse model, for small frequency wavelets (10–20 Hz), the vertical resolution is low (Fig. 11, first and second rows). The reflectors are continuous in the vertical and horizontal direction, which make difficult to distinguish the sandstone and shale layers or to interpret the normal fault (Fig. 11, first and second rows). For specular illumination, the top reflector is continuous, and for the left and right side illuminations, amplitude values are low (Fig. 11, first and second rows). From 30 Hz and higher frequencies, the two shale layers are distinguishable and the diffractions associated to the fault are visible (Fig. 11, third and fourth rows). Breaks or offsets in the layer boundaries, are marked by low amplitude values in the images produced by specular illumination, and by diffracted energy in the images produced by footwall or hanging wall directed illumination (Fig. 11, third and fourth rows).

For the fine model, at low frequency (10 Hz) the resulting seismic images (Fig. 12, first and second rows) are almost identical to those of the coarse model (Fig. 11, first and second rows). However, amplitude values are slightly higher for the fine model where the main fault is closer to a single plane. From 20 Hz, the fault structure and irregular geometry of the layer boundaries are more evident (Fig. 12, second row). At 30 and 40 Hz, the impact of the smaller fault segment is visible mostly in the upper shale layer in the three illumination images, and the diffracted energy is more important for the left and right side illuminations (Fig. 12, third and four rows).

3.2.3. Reflector geometry and associated amplitude

In an attempt to perform a more quantitative interpretation of the seismic images, we extract the amplitude values along selected profiles in the seismic images produced by specular illumination (Figs. 11 and 12, first column). Although there are several seismic attributes that help in the interpretation and characterization of

faults (e.g., Dutzer et al., 2010; Iacopini and Butler, 2011; Iacopini et al., 2012), we decided to focus only on the amplitude response of the fault zone at several wave frequencies as a proof of concept of our workflow. The selected profiles correspond to the interpreted top interfaces of the shale layers in the seismic images (Figs. 13b and 14b). The extraction of the amplitudes was performed in a window 10 m above and below the interpreted reflector, using a root mean square (RMS) computation, and for wave frequencies from 10 to 40 Hz (Figs. 13a and c, and 14a and c). The amplitude profiles are compared to the RMS input elastic properties along the same interpreted reflector paths, in order to evaluate the correlation between amplitude anomalies and variations of elastic properties controlled by fault structure. For comparison, the RMS amplitude, density, and P-wave velocity are all scaled from 0 to 1 (Figs. 13a and c, and 14a and c).

In the coarse model (Fig. 13), the geometry of the interpreted reflector changes with the frequency of the wavelet (Fig. 13b): the higher the wave frequency is, the better the interpreted reflector matches the shale/sandstone interface and more information can be obtained about the structure of the fault (Fig. 13). RMS amplitudes (black lines in Fig. 13a and c) are similar for the interpreted upper and lower reflectors at 10 Hz (Fig. 13a and c, first column). From 20-Hz, there are differences due to higher dips of the interpreted lower reflector in the fault zone, which leads to higher relative changes in amplitude over shorter distances (Fig. 13 a and c, second to fourth columns). At relatively high frequencies (30–40 Hz), the interpreted lower reflector shows an offset, which is represented in the amplitude profile by a sharp drop right before the offset, followed by a sharp increase after the offset. The split of the fault into two segments is also visible in the interpreted upper reflector at these high frequencies, where it is defined by a pair of amplitude lows and highs (Fig. 13a and c, third and fourth columns).

The specular seismic images for the fine model (Fig. 14) present similar characteristics than those for the coarse model. The accuracy of the interpreted reflector geometry in following the actual

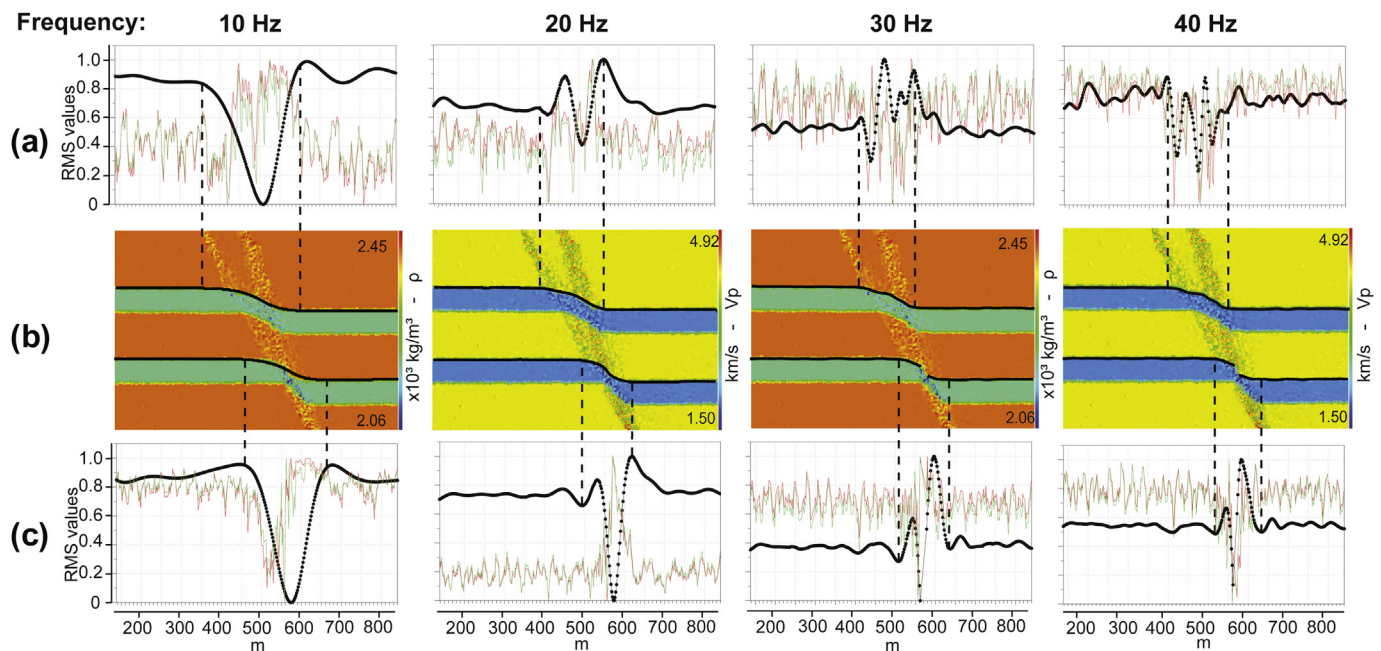


Figure 13. RMS amplitude (black line) and RMS property (density in red and P-wave velocity in green) along a swath 10 m above and below the interpreted top of the upper (a) and lower (c) shale layers, in the seismic profile with specular illumination of the normal fault coarse model (Fig. 11, left column). (b) Density ρ , P-wave velocity V_p and interpreted reflectors (black lines). The four columns in (a) and (c) correspond to different frequencies of an incoming zero-phase Ricker pulse: 10 (first column), 20 (second column), 30 (third column), and 40 Hz (fourth column). Dotted lines in (a) and (c) indicate the area of influence of the fault. (For interpretation of the references to color in this figure legend, the reader is referred to the web version of this article.)

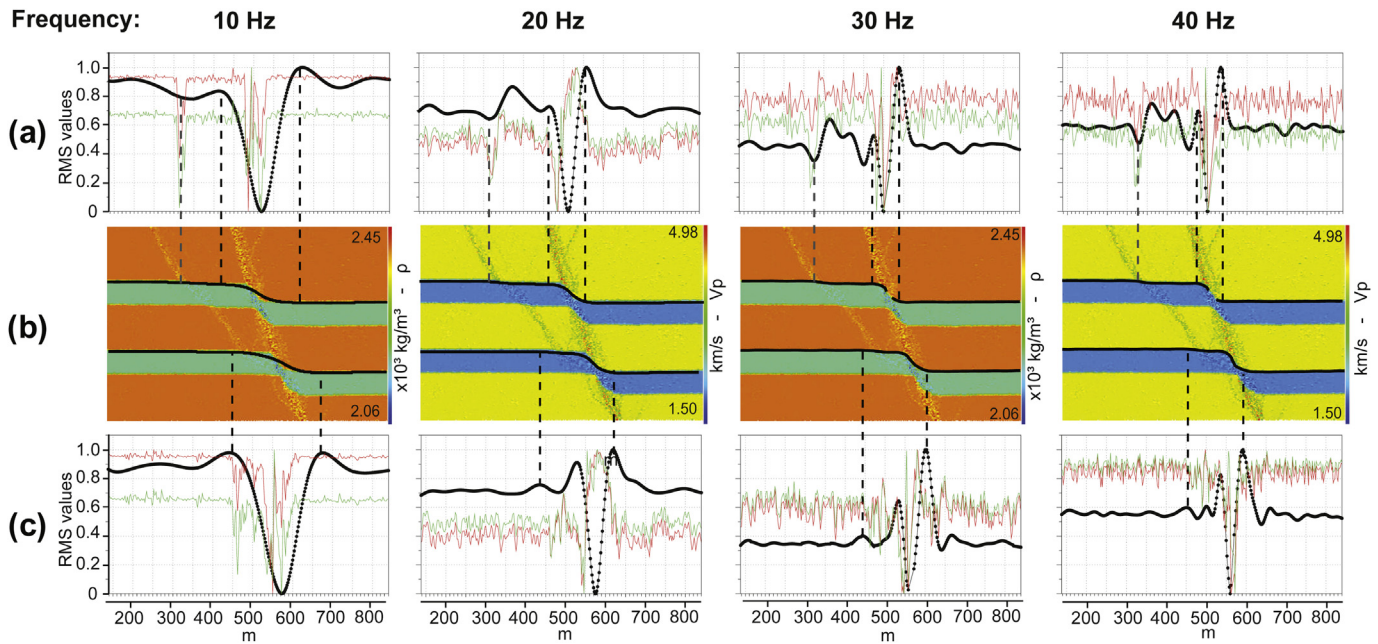


Figure 14. RMS amplitude (black line) and RMS property (density in red and P-wave velocity in green) along a swath 10 m above and below the interpreted top of the upper (a) and lower (c) shale layers, in the seismic profile with specular illumination of the normal fault fine model (Fig. 12, left column). (b) Density ρ , P-wave velocity V_p and interpreted reflectors (black lines). The four columns in (a) and (c) correspond to different frequencies of an incoming zero-phase Ricker pulse: 10 (first column), 20 (second column), 30 (third column), and 40 Hz (fourth column). Dotted lines in (a) and (c) indicate the area of influence of the fault. (For interpretation of the references to color in this figure legend, the reader is referred to the web version of this article.)

shale/sandstone boundary increases with the frequency (Fig. 14). At a wave frequency of 10 Hz, the interpreted reflectors geometry and the extracted RMS amplitudes are very similar to those of the coarse model, with no further details of fault structure (Fig. 14a and c, first column). From 20 Hz wave frequencies, the second smaller fault segment is indicated by amplitude changes, especially in the interpreted upper reflector, (Fig. 14a and c, second column). At 30 and 40 Hz, the offset of the upper reflector by the main fault, is shown by a trough and peak in the amplitude profile. A smaller trough and peak in the amplitude profile also mark the smaller fault segment (Fig. 14a, third and fourth columns). The interpreted lower reflector has approximately the same geometry and RMS amplitude variations than in the coarse model (Figs. 14b–c and 13b–c).

3.2.4. Amplitude and elastic properties correlation

Figures 13 (a and c) and 14 (a and c) show the variation of the input RMS density (red lines in the web version) and P-wave velocity (green lines in the web version) along the interpreted reflectors for a window of 10 m above and below the reflector. The shear-wave velocity is not presented, because it is directly related to the P-wave velocity (Equation (4)). In the coarse model, changes in density and P-wave velocity in the fault zone correlate well with amplitude changes (Fig. 13). This correlation increases with wave frequency. Along the interpreted upper reflector at a wave frequency of 10 Hz, the presence of two fault segments is clear in the density and P-wave velocity profiles, but not in the amplitude profile (Fig. 13a, first column). From 20 Hz, the changes of acoustic properties and amplitude are approximately in phase (Fig. 13a, second column). At 30 and 40 Hz, a pair of troughs and highs in both the acoustic properties and amplitude profiles clearly indicates the two fault segments (Fig. 13a, third and fourth columns). At these high frequencies amplitude and acoustic properties variations are practically in phase. Along the interpreted lower reflector at low wave frequencies of 10–20 Hz, the relative changes of acoustic properties and amplitude are almost similar, although the

acoustic properties and amplitude variations are out of phase at 10 Hz (Fig. 13c, first and second columns). From 30 Hz, a trough and peak in both the acoustic properties and amplitude profiles mark the offset of the lower reflector (Fig. 13c, third and fourth columns). The acoustic properties fluctuations, however, are larger than those of the amplitude. At 40 Hz, the amplitude variation correlates well with the changes in acoustic properties (Fig. 13c, fourth column).

The higher resolution of the fine model results in smaller fluctuations in acoustic properties along the interpreted reflectors than those for the coarse model (Fig. 14). Along the interpreted upper reflector at low wave frequencies of 10–20 Hz, the smaller fault segment clearly marked by the acoustic properties variations, is less detectable in the amplitude profiles. An abrupt drop in both acoustic properties and amplitude indicates the main fault segment, although amplitude and acoustic properties are slightly out of phase (Fig. 14a, first and second columns). At 30 and particularly 40 Hz, the acoustic properties and amplitude variations correlate well. Both, the smaller and main fault segments are visible (Fig. 14a, third and fourth columns). Along the interpreted lower reflector, the profiles of acoustic properties and amplitude are similar to those of the coarse model, but with smaller fluctuations (Fig. 14c). A large drop in acoustic properties and amplitude mark the main fault, although acoustic properties and amplitude are out of phase at low frequencies of 10–20 Hz (Fig. 14c, first and second columns). At higher frequencies of 30 and particularly 40 Hz, acoustic properties and amplitude variations are in phase and correlate well (Fig. 14c, third and fourth columns). Interestingly, neither the acoustic properties nor the amplitude variations at any of the chosen frequencies seem to indicate a second fault segment in the lower reflector (Fig. 14c).

Overall, Figures 13 and 14 show that the correlation between amplitude and acoustic properties variations increases with wave frequency and the accuracy of the interpreted reflector. The amplitude profiles allow determining the lateral extent of fault related deformation (i.e. the fault zone) at the level of the

interpreted reflector (dotted black lines in Figs. 13 and 14). Changes in acoustic (and petrophysical) properties in the fault zone can also be determined from the amplitude variations (Figs. 13 and 14). For the coarse and fine models, the maximum changes in RMS amplitude (troughs and peaks) in the main fault segment correspond to changes of 20–25% in P-wave velocity from the host rock values (Figs. 7 and 10). This is a direct result of the assumed correlation between P-wave velocity variation and volumetric finite strain (Fig. 3). For the fine model, changes in amplitude in the small fault segment correspond to changes of 10–15% in P-wave velocity (Fig. 10). Changes in density are lower than changes in seismic velocities. In the largest troughs and peaks of the amplitude profiles for the coarse and fine models (Figs. 13 and 14), changes in porosity are 20–25% (Fig. 3). This corresponds to density changes of about 4–5% (Equation (2) and Table 3). This knowledge of the extent of fault related deformation as well as of the relative changes of rock properties in the fault zone is critical for the assessment of the sealing capacity of the fault.

4. Discussion and conclusions

We have presented a synthetic methodology to study the impact of fault zone structure on seismic images. Fault evolution was simulated with a DEM, which allowed us to study faulting at large scale and the impact on fault deformation of parameters such as rock competence, overburden stress, fault displacement and particle size. Although the mechanical behavior of the DEM is purely frictional (i.e., no unconfined compressive strength and no tensile strength) and particle sizes are large in the coarse and fine models, the models were able to capture complex features of fault evolution and produce realistic fault geometries and strain fields. Both models display a fault zone initially consisting of isolated fault segments that later link. Particle size controls fault evolution, with the fine model displaying narrower fault zones and fault linkage at later stages. This behavior is also observed in sand and clay analogue models of faulting (Eisenstadt and Sims, 2005). The differences between the coarse and fine models can be seen as a numerical issue resulting from the particle sizes. However, they can also reflect reality. Smaller particles or grains allow more localization. The range of particle sizes can therefore be used as an advantage to simulate a large spectrum of fault geometries and strain fields observable in nature. Our DEM models do not have the complexity of the smaller-scale, bonded DEM models of Schöpfer et al. (2007), which require high tensile strengths; or the resolution of the DEM models of Egholm et al. (2008), which focus on clay smearing at the outcrop scale. The role of different loading configurations, which can produce similar fault geometry but dissimilar incremental and permanent strain (Lewis et al., 2007) is also not considered.

Seismic imaging requires an input cube of elastic properties (density, V_P and V_S). However after faulting, these properties are difficult to retrieve. The effect of large, permanent strain on elastic properties is poorly understood. At the magnitudes of finite strain in fault zones, simple linear laws that relate stress to strain such as elasticity are not applicable, and finite strain is the main reliable variable that we can take into account. The presented DEM models do not address processes at the grain scale and so there are challenges relating laboratory studies to the bulk mechanical behavior of the DEM. Therefore, the estimation of the changes of seismic properties due to finite strain has to be simple and empirical due to the complexity of the problem. As stated by Hatchell and Bourne (2005) and Couples et al. (2007), a simple relationship between permanent strain and acoustic properties at large scale, although probably inaccurate, is sufficient to assess the impact of faulting on seismic data. Equations 1–4 allow computing

the change of seismic properties with finite volumetric strain in the modeled fault zone. In the future, we could add more information to the link between geomechanics and seismic modeling, such as the impact of shear strain and fracturing on seismic properties. However, we most probably still have to rely on empirical relations to link these two.

The application of the PSDM simulator to the mechanically derived reflectivity field provides a way to evaluate the acquisition and processing parameters required to better image the fault zone. Even if the ray-based PSDM simulator relies on some assumptions (e.g. single scattering and local plane wavenumber), the sensitivity analysis introduced here approaches closer the reality of seismic acquisition and processing than industry standard, post-stack seismic modeling techniques such as 1D convolution. The two parameters presented, illumination direction and frequency, already include survey geometry, wave type, background media and overburden, all of which have a large impact on the seismic image. Other parameters and more complex cases (e.g., lateral variations in overburden) will be considered in future work. In both the coarse and fine normal fault models with specular illumination, higher wave frequencies (30 Hz and more) result in better definition and higher diffracted energy from the fault zone (Figs. 11 and 12, first column). The diffraction part of the seismic energy really helps to characterize the fault zone. Diffractions make possible determining the lateral and vertical extent of faulting without focusing only on reflector offsets (Figs. 11 and 12, first column). The depth of our model (about 1.5 km) is shallow in conventional seismic. At this depth, the typical dominant frequency can be higher than 30 Hz. For reservoirs deeper than 3 km (which is a typical case in the North Sea), it is sometimes difficult to obtain frequencies higher than 30 Hz, and reflections can hide details of the fault structure. Changing the illumination direction can help to highlight the internal structure of the fault zone, and therefore this parameter can be tested during seismic acquisition for specific fault characterization. Side illumination targets directly the fault plane. Hanging wall side illumination shows well the structure of the main fault zone, but not the smaller fault segment in the footwall of the main fault (Figs. 11 and 12, third column). Footwall side illumination results in low amplitude images, however, only this illumination makes the smaller fault segment of the fine model visible (Fig. 12, second column). Both frequency and illumination direction are important for imaging the fault zone.

This work emphasizes the impact of fault zone internal structure on the resultant seismic image. Indeed, the general interpretation of faults as 2D surfaces is too simplistic. Figure 15 shows a comparison between the coarse model (Fig. 15a), the fine model (Fig. 15b), and a planar 60° dipping normal fault model (Fig. 15c). The planar fault model (Fig. 15c, left) represents how faults are typically interpreted; with only reflector offsets and no fault related strain (folding, minor faulting, fracturing, etc.). Seismic images for a 40 Hz, zero-phase Ricker pulse, a 1.5 km homogeneous overburden with a P-wave velocity of 4 m/s, and three illumination patterns are presented for the three models (Fig. 15a–c, second to fourth columns). Even though the general aspect of the seismic images is similar, there are clear differences between them. For the specular illumination images, diffractions are critical to delimit the extent of faulting in the coarse and fine models (Fig. 15a–b, second column), and should be used to guide the correct interpretation of faults in seismic data. Diffractions, however, are almost absent in the planar fault model (Fig. 15c, second column). For the side illumination images, reflections are continuous outside the main fault in the planar fault model (Fig. 15c, third and fourth columns), but are discontinuous and display more amplitude variability in the coarse and fine models (Fig. 15a–b, third and fourth columns). For the hanging wall side illumination, it is interesting to see how the

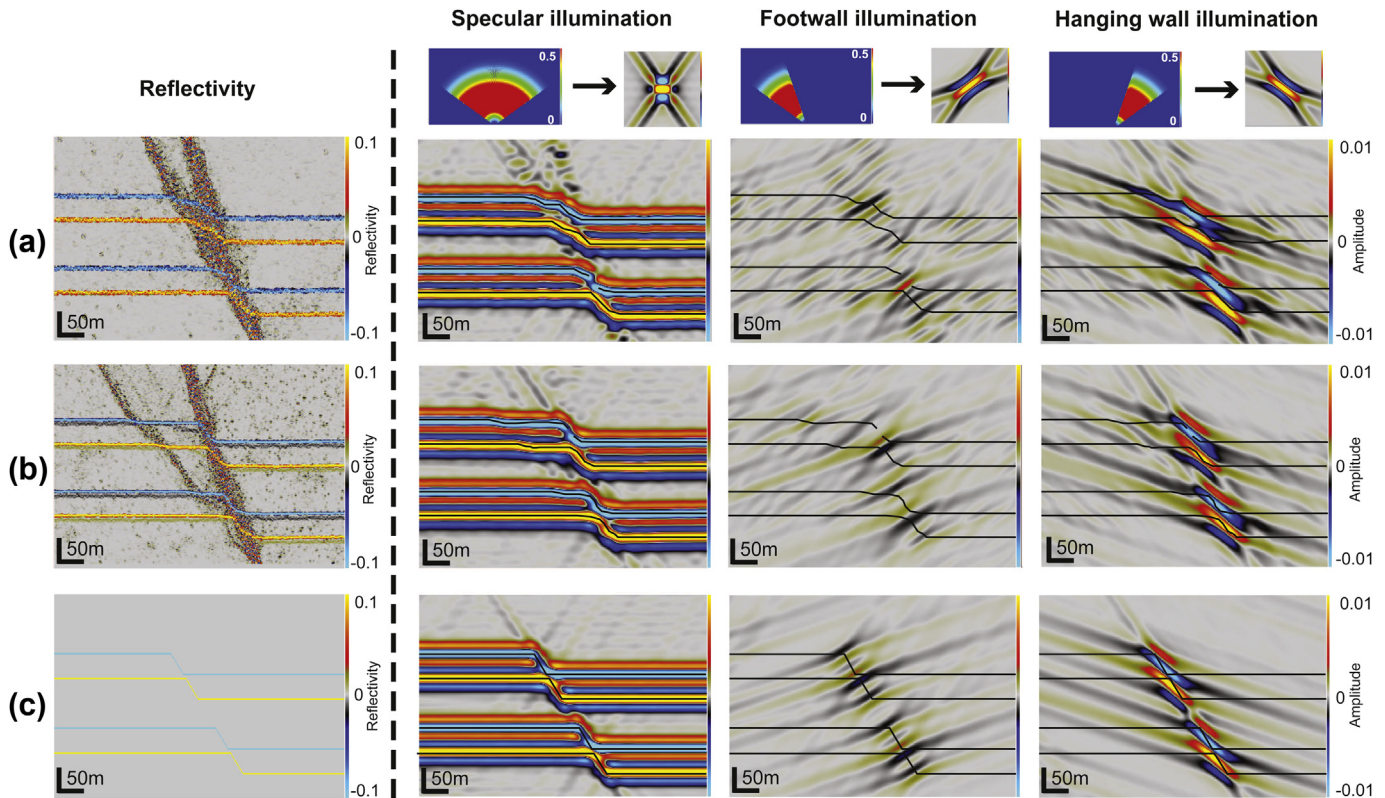


Figure 15. Seismic profiles of (a) Normal fault coarse model, (b) Normal fault fine model, and (c) Planar normal fault model. First column is the input reflectivity. Second to fourth columns correspond to different illumination directions: Specular (second column), from footwall (third column), and from hanging wall (fourth column). The seismic images were generated with a 40 Hz, zero-phase Ricker pulse. The overburden is 1.5 km and is homogeneous. Black lines in second to fourth columns are layer boundaries.

width of the high amplitude reflections in the fault zone decreases from the coarse model (Fig. 15a, fourth column), to the fine model (Fig. 15b, fourth column), and to the planar fault model (Fig. 15c, fourth column); giving a clear indication of the thickness of the fault zone.

The analysis of RMS amplitude along interpreted reflectors helps defining the architecture of the fault zone. The higher the frequency band is, the closer the interpreted reflectors are to the layer boundaries and the better the definition of fault architecture (Figs. 13 and 14). However, at high wave frequencies, e.g. 40 Hz, the interpreted reflector and its associated RMS amplitude can capture small fluctuations of the layer interface, which may interfere with the interpretation of the fault geometry. For example in the fine model, it can be difficult to distinguish the smaller fault segment along the interpreted lower shale/sandstone interface at 40-Hz (Fig. 14c, fourth column). When working at high frequencies, the interpreter may need to disregard small amplitude variations (e.g. small layer fluctuations), and focus on larger amplitude changes that may indicate faulting (e.g. the slightly higher peak defining the smaller fault segment in Fig. 14c, fourth column).

In our synthetic modeling, changes in RMS amplitude along the interpreted reflectors are directly correlated to changes in acoustic properties, especially at high wave frequencies (Figs. 13 and 14, third and fourth columns). This may provide a way to estimate the changes in acoustic properties in the fault zone with respect to the host rock, but pending that amplitudes have been properly preserved while processing and imaging. Seismic amplitude (black lines in Figs. 13 and 14), although displaying less variability than the input acoustic properties (red and green lines in Figs. 13 and 14), gives an estimate of the average gradient of change and maximum change of acoustic properties in the fault zone. Even though RMS

amplitude was the only attribute used for the qualitative interpretation of the seismic images, this information is critical for reconstructing the distribution of rock properties in the fault zone. Although acoustic and fluid flow (e.g., permeability) rock properties are not directly correlated, contrast changes of seismic amplitude across faults could be a direct indicator of the permeability distribution, which will be critical for determining fault sealing. The study of more seismic attributes (e.g. dip and azimuth, curvature, coherence or tensor, Dutzer et al., 2010) could help to a better definition of the petrophysical properties of the model, but require a deeper investigation of the relation between the seismic data and each of these properties.

The proposed workflow is a step forward towards the seismic characterization of complex fault zones. The coarse and fine DEM models give insight on fault evolution at large scales. Sensitivity analyses of two seismic parameters, illumination direction and wave frequency, give information on how to handle seismic data for fault interpretation: During acquisition (e.g., by focusing on an illumination from the hanging wall rather than from the footwall), processing (e.g., by focusing on diffracted rather than reflected energy), and interpretation (e.g., by analyzing amplitude variations). The methodology is here presented as a proof of concept in 2D, but it can be extended to 3D. 2D does not allow us to investigate several factors that are key during faulting, including variations of fault geometry (e.g. fault dip) and fault displacement, and fault propagation and linkage along strike. In an actual faulted volume, a single illumination direction is most probably not sufficient to image the fault network. Ongoing work is focusing on running such 3D simulations. These simulations allow us to explore additional geologic processes such as changes of fault displacement and fault interaction along strike, plus exploiting the true potential of the

PSDM simulator with realistic surveys, overburdens, etc. The validity of seismic attributes analyses to determine the extent of fault damage, isolate the fault damage volume, and predict its internal architecture and properties (Dutzer et al., 2010), can also be evaluated. Future work will also include seismic imaging simulations of a real 3D case scenario (e.g. outcrop) with well-constrained fault related deformation and petrophysical properties (e.g., Rotevatn and Fossen, 2011).

Acknowledgments

This work was funded by the Norwegian Research Council through the project “Seismic Imaging of Fault Zones” (NFR-PET-ROMAKS, project no. 210425/E30). Mechanical modeling was performed using the program cdem2D by Stuart Hardy, finite strain was computed using the program SSPX by Nestor Cardozo and Richard Allmendinger, seismic imaging simulation was performed in SeisRoX (NORSAR), and analysis of seismic amplitudes was done in Petrel (Schlumberger).

References

- Abe, S., van Gent, H., Urai, J.L., 2011. DEM simulation of normal faults in cohesive materials. *Tectonophysics* 512, 12–21.
- Allmendinger, R.W., Cardozo, N., Fisher, D., 2012. *Structural Geology Algorithms: Vectors and Tensors*. Cambridge University Press, 302 p.
- Aarland, R.K., Skjerven, J., 1998. Fault and fracture characteristics of a major fault zone in the northern North Sea: analysis of 3D seismic and oriented cores in the Brage Field (Block 31/4). In: Geological Society, London, Special Publications, vol. 127, pp. 209–229.
- Bastesen, E., Braathen, A., 2010. Extensional faults in fine grained carbonates – analysis of fault core lithology and thickness-displacement relationships. *J. Struct. Geol.* 32, 1609–1628.
- Ben-Zion, Y., Peng, Z., Okaya, D., Seeber, L., Armbruster, J.G., Ozer, N., Michael, A.J., Baris, S., Aktar, M., 2003. A shallow fault-zone structure illuminated by trapped waves in the Karadere-Duzce branch of the North Anatolian Fault, western Turkey. *Geophys. J. Int.* 152, 699–717.
- Cardozo, N., Allmendinger, R.W., 2009. SSPX: a program to compute strain from displacement/velocity data. *Comput. Geosci.* 35, 1343–1357.
- Childs, C., Watterson, J., Walsh, J.J., 1996. A model for the structure and development of fault zones. *J. Geol. Soc. Lond.* 153, 337–340.
- Childs, C., Manzocchi, T., Walsh, J.J., Bonson, C.G., Nicol, A., Schöpfer, M.P.J., 2009. A geometric model of fault zone and fault rock thickness variations. *J. Struct. Geol.* 31, 117–127.
- Couples, G., Ma, J., Lewis, H., Olden, P., Quijano, J., Fasaie, T., Maguire, R., 2007. Geomechanics of faults: impacts on seismic imaging. *First Break* 25, 83–90.
- Cundall, P.A., Strack, O.D.L., 1979. A discrete numerical model for granular assemblies. *Geotechnique* 29, 47–65.
- Davatzes, N.C., Eichhubl, P., Aydin, A., 2005. Structural evolution of fault zones in sandstone by multiple deformation mechanisms: Moab fault, southeast Utah. *GSA Bull.* 117, 135–148.
- Drottning, Å., Branston, M., Lecomte, I., 2009. Value of illumination-consistent modeling in time-lapse seismic analysis. *First Break* 27 (10), 75–83.
- Dutzer, J.F., Basfor, H., Purves, S., 2010. Investigating fault sealing potential through fault relative seismic volume analysis. *Petroleum Geology Conference*. In: The Geological Society, London, vol. 7, pp. 509–515.
- Egholm, D.L., Sandiford, M., Clausen, O.R., Nielsen, S.B., 2007. A new strategy for discrete element numerical models: 2. Sandbox applications. *J. Geophys. Res.* 112, B05204 <http://dx.doi.org/10.1029/2006JB004558>.
- Egholm, D.L., Clausen, O.R., Sandiford, M., Kristensen, M.B., Korstgård, J.A., 2008. The mechanics of clay smearing along faults. *Geology* 36, 787–790.
- Eichhubl, P., D'Onfro, P.S., Aydin, A., Waters, J., McCarty, D.K., 2005. Structure, petrophysics, and diagenesis of shale entrained along a normal fault at Black Diamond Mines, California – implications for fault seal. *AAPG Bull.* 89, 113–1137.
- Eisenstadt, G., Sims, D., 2005. Evaluating sand and clay models: do rheological differences matter? *J. Struct. Geol.* 27, 1399–1412.
- Faulkner, D.R., Jackson, C.A.L., Lunn, R.J., Schlische, R.W., Shipton, Z.K., Wibberley, C.A.J., Withjack, M.O., 2010. A review of recent developments concerning the structure, mechanics and fluid flow properties of fault zones. *J. Struct. Geol.* 32, 1557–1575.
- Finch, E., Hardy, S., Gawthorpe, R.L., 2004. Discrete element modelling of extensional fault-propagation folding above rigid basement fault blocks. *Basin Res.* 16, 489–506.
- Fisher, Q.J., Knipe, R.J., 1998. Fault sealing processes in siliciclastic sediments. In: Jones, G., Fisher, Q.J., Knipe, R.J. (Eds.), *Faulting, Fault Sealing and Fluid Flow in Hydrocarbon Reservoirs*, Geological Society, London, Special Publications, vol. 147, pp. 117–134.
- Foxford, K.A., Walsh, J.J., Watterson, J., Garden, I.R., Guscott, S.C., Burley, S.D., 1998. Structure and content of the Moab Fault Zone, Utah, USA, and its implications for fault seal prediction. In: Jones, G., Fisher, Q.J., Knipe, R.J. (Eds.), *Faulting, Fault Sealing and Fluid Flow in Hydrocarbon Reservoirs*, Geological Society, London, Special Publications, vol. 147, pp. 87–103.
- Færseth, R.B., 2006. Shale smear along large faults: continuity of smear and the fault seal capacity. *J. Geol. Soc. Lond.* 163, 741–751.
- Gray, G.G., Morgan, J.K., Sanz, P.F., 2014. Overview of continuum and particle dynamics methods for mechanical modeling of contractional geologic structures. *J. Struct. Geol.* 59, 19–36.
- Gjøystdal, H., Iversen, E., Lecomte, I., Kaschwish, T., Drottning, Å., Mispel, J., 2007. Improved applicability of ray tracing in seismic acquisition, imaging, and interpretation. *Geophysics* 72, SM261–SM271.
- Hardy, S., 2008. Structural evolution of calderas: insights from two-dimensional discrete element simulations. *Geology* 36, 927–930.
- Hardy, S., 2011. Cover deformation above steep, basement normal faults: insights from 2D discrete element modeling. *Mar. Pet. Geol.* 28, 966–972.
- Hardy, S., 2013. Propagation of blind normal faults to the surface in basaltic sequences: insights from 2D discrete element modelling. *Mar. Pet. Geol.* 48, 149–159.
- Hardy, S., Finch, E., 2005. Discrete-element modelling of detachment folding. *Basin Res.* 17, 507–520.
- Hardy, S., Finch, E., 2006. Discrete element modelling of the influence of cover strength on basement-involved fault-propagation folding. *Tectonophysics* 415, 225–238.
- Hardy, S., McClay, K., Anton Muñoz, J.A., 2009. Deformation and fault activity in space and time in high-resolution numerical models of doubly vergent thrust wedges. *Mar. Pet. Geol.* 26, 232–248.
- Hatchell, P., Bourne, S., 2005. Rocks under strain: strain-induced time-lapse time shifts are observed for depleting reservoirs. *Lead. Edge* 24, 1222–1225.
- Hoek, E., Brown, E.T., 1997. Practical estimates of rock mass strength. *Int. J. Rock Mech. Min. Sci.* 34, 1165–1186.
- Holohan, E.P., Schöpfer, M.P.J., Walsh, J.J., 2011. Mechanical and geometric controls on the structural evolution of pit crater and caldera subsidence. *J. Geophys. Res.* 116, B07202 [doi:10.1029/2010JB008032](http://dx.doi.org/10.1029/2010JB008032).
- Holt, R.M., Fjaer, E., Nes, O.M., Stenebraten, J.F., 2008. Strain sensitivity of wave velocities in sediments and sedimentary rocks. In: *The 42nd US Rock Mechanics Symposium (USRMS)*. American Rock Mechanics Association.
- Horsrud, P., Sønstebo, E.F., Bøe, R., 1998. Mechanical and petrophysical properties of North Sea shales. *Int. J. Rock Mech. Min. Sci.* 35, 1009–1020.
- Hubbert, M.K., 1951. Mechanical basis for certain familiar geologic structures. *GSA Bull.* 62, 355–372.
- Iacopini, D., Butler, R., 2011. Imaging deformation in submarine thrust belts using seismic attributes. *Earth Planet. Sci. Lett.* 302, 414–422.
- Iacopini, D., Butler, R., Purves, S., 2012. Seismic imaging of thrust faults and structural damage: a visualization workflow for deepwater thrust belts. *First Break* 30, 77–84.
- Jeanne, P., Guglielmi, Y., Cappa, F., 2012. Multiscale seismic signature of a small fault zone in a carbonate reservoir: relationships between VP imaging, fault zone architecture and cohesion. *Tectonophysics* 554–557, 185–201.
- Kaschwish, T., Gjøystdal, H., Lecomte, I., 2011. Impact of diffraction on resolution of PSDM, extended abstract. In: *73rd EAGE Conference & Exhibition incorporating SPE EUROPEC 2011*, Vienna, Austria, 23–26 May, P384.
- Koledoye, B.A., Aydin, A., May, E., 2003. A new process-based methodology for analysis of shale smear along normal faults in the Niger Delta. *AAPG Bull.* 87, 445–463.
- Lecomte, I., Kaschwish, T., 2008. Closer to Real Earth in Reservoir Characterization: a 3D Isotropic/Anisotropic PSDM Simulator. 2008 SEG Annual Meeting, 9–14 November. Society of Exploration Geophysicists, Las Vegas, Nevada.
- Lecomte, I., 2008. Resolution and illumination analyses in PSDM: a ray-based approach. *Lead. Edge* 27, 650–663.
- Lewis, M.A., Peng, Z., Ben-Zion, Y., Vernon, F.L., 2005. Shallow seismic trapping structure in the San Jacinto fault zone near Anza, California. *Geophys. J. Int.* 162, 867–881.
- Lewis, H., Hall, S.A., Guest, J., Couples, G.D., 2007. Kinematically-equivalent but geomechanically-different simulations of fault evolution: the role of loading configurations. In: Jolley, S.J., Barr, D., Walsh, J.J., Knipe, R.J. (Eds.), *Structurally Complex Reservoirs*, Geological Society, London, Special Publications, vol. 292, pp. 159–172.
- Li, X., Liu, Y., Liu, E., Shen, F., Qi, L., Shouli, Q., 2003. Fracture detection using land 3D seismic data from the Yellow River Delta, China. *Lead. Edge* 22, 680–683.
- Long, J.J., Imber, J., 2010. Geometrically coherent continuous deformation in the volume surrounding a seismically imaged normal fault-array. *J. Struct. Geol.* 32, 222–234.
- Long, J.J., Imber, J., 2012. Strain compatibility and fault linkage in relay zones on normal faults. *J. Struct. Geol.* 36, 16–26.
- Manzocchi, T., Childs, C., Walsh, J.J., 2010. Faults and fault properties in hydrocarbon flow models. *Geofluids* 10, 94–113.
- Mavko, G., Mukerji, T., Dvorkin, J., 2009. *The Rock Physics Handbook: Tools for Seismic Analysis in Porous Media*, second ed. Cambridge University Press, New York.
- Mora, P., Place, D., 1993. A lattice solid model for the non-linear dynamics of earthquakes. *Int. J. Mod. Phys. C* 4, 1059–1074.

- Nygård, R., Gutierrez, M., Bratli, R.K., Høeg, K., 2006. Brittle-ductile transition, shear failure and leakage in shales and mudrocks. *Mar. Pet. Geol.* 23, 201–212.
- Oger, L., Savage, S.B., Corriveau, D., Sayed, M., 1998. Yield and deformation of an assembly of disks subject to a deviatoric stress loading. *Mech. Mater.* 27, 189–210.
- Rotevatn, A., Fossen, H., 2011. Simulating the effect of subseismic fault tails and process zones in a siliciclastic reservoir analogue: implications for aquifer support and trap definition. *Mar. Pet. Geol.* 28, 1648–1662.
- Schöpfer, M.P.J., Childs, C., Walsh, J.J., 2007. Two-dimensional distinct element modeling of the structure and growth of normal faults in multilayer sequences: 1. Model calibration, boundary conditions, and selected results. *J. Geophys. Res.* 112 (10), B10401.
- Shtivelman, V., Marco, S., Reshef, M., Agnon, A., Hamiel, Y., 2005. Using trapped waves for mapping shallow fault zones. *Near Surf. Geophys.* 3, 91–97.
- Sigernes, L.-T.W., 2004. Rock Physics of Extensional Faults and Their Seismic Imaging Properties (Doctoral thesis, monograph). Norwegian University of Science and Technology, 305 p.
- Skurveit, E., Torabi, A., Gabrielsen, R.H., Zoback, M.D., 2013. Experimental investigation of deformation mechanisms during shear-enhanced compaction in poorly lithified sandstone and sand. *J. Geophys. Res. Solid Earth* 118, 4083–4100.
- Solum, J.G., Davatzes, N.C., Lockner, D.A., 2010. Fault-related clay authigenesis along the Moab Fault: implications for calculations of fault rock composition and mechanical and hydrologic fault zone properties. *J. Struct. Geol.* 32, 1899–1911.
- Terhegge, J.H., Wassing, B.B.T., Orlic, B., Giger, S.B., Clennell, M.B., 2013. Constraints on the sealing capacity of faults with clay smears from discrete element models validated by laboratory experiments. *Rock Mech. Rock Eng.* 46, 465–478.
- Thompson, N., Bennett, M.R., Petford, N., 2010. Development of characteristic volcanic debris avalanche deposit structures: new insights from distinct element simulations. *J. Volcanol. Geotherm. Res.* 192, 191–200.
- Townsend, C., Firth, I.R., Westerman, R., Kirkevollen, L., Hårde, M., Andersen, T., 1998. Small seismic-scale fault identification and mapping. In: Jones, G., Fisher, Q.J., Knipe, R.J. (Eds.), *Faulting, Fault Sealing and Fluid Flow in Hydrocarbon Reservoirs*, Geological Society, London, Special Publications, vol. 147, pp. 1–25.
- van Gent, H.W., Holland, M., Urai, J.L., Loosveld, R., 2010. Evolution of fault zones in carbonates with mechanical stratigraphy - insights from scale models using layered cohesive powder. *J. Struct. Geol.* 32, 1375–1391.
- Wibberley, C.A.J., Yielding, G., Di Toro, G., 2008. Recent advances in the understanding of fault zone internal structure: a review. In: Wibberley, C.A.J., Kurz, W., Imber, J., Holdsworth, R.E., Colletini, C. (Eds.), *The Internal Structure of Fault Zones: Implications for Mechanical and Fluid-flow Properties*, Geological Society, London, Special Publications, vol. 299, pp. 5–33.
- Yielding, G., Bretan, P., Freeman, B., 2010. Fault seal calibration: a brief review. In: Jolley, S.J., Fisher, Q.J., Ainsworth, R.B., Vrolijk, P.J., Delisle, S. (Eds.), *Reservoir Compartmentalization*, Geological Society, London, Special Publications, vol. 347, pp. 243–255.
- Zhang, J., Morgan, J.K., Gray, G.G., Harkins, N.W., Sanz, P.F., Chikichev, I., 2013. Comparative FEM and DEM modeling of basement-involved thrust structures, with application to Sheep Mountain, Greybull area, Wyoming. *Tectonophysics* 608, 408–417.
- Zoback, M.D., 2010. *Reservoir Geomechanics*. Cambridge University Press, 461 p.
- Zühlsdorff, L., Gjøystdal, H., Drottning, Å., Lecomte, I., Moen, S.I., Bolin, H., 2013. Modern ray-based modelling and simulated depth migration for survey planning and interpretation: a 3D VSP example. *Geohorizons* 18 (2), 27–37.